



Search for nonresonant pair production of Higgs bosons in the $b\bar{b}b\bar{b}$ final state in pp collisions at $\sqrt{s} = 13$ TeV with the ATLAS detector

The ATLAS Collaboration

A search for nonresonant Higgs boson pair production in the $b\bar{b}b\bar{b}$ final state is presented. The analysis uses 126 fb^{-1} of pp collision data at $\sqrt{s} = 13$ TeV collected with the ATLAS detector at the Large Hadron Collider, and targets both the gluon–gluon fusion and vector-boson fusion production modes. No evidence of the signal is found and the observed (expected) upper limit on the cross-section for nonresonant Higgs boson pair production is determined to be 5.4 (8.1) times the Standard Model predicted cross-section at 95% confidence level. Constraints are placed on modifiers to the HHH and $HHVV$ couplings. The observed (expected) 2σ constraints on the HHH coupling modifier, κ_λ , are determined to be $[-3.5, 11.3]$ ($[-5.4, 11.4]$), while the corresponding constraints for the $HHVV$ coupling modifier, κ_{2V} , are $[-0.0, 2.1]$ ($[-0.1, 2.1]$). In addition, constraints on relevant coefficients are derived in the context of the Standard Model effective field theory and Higgs effective field theory, and upper limits on the HH production cross-section are placed in seven Higgs effective field theory benchmark scenarios.

1 Introduction

The discovery of the 125 GeV Higgs boson (H) [1–4] at the Large Hadron Collider (LHC) has prompted a broad research program to investigate its properties and compare the measurements with the Standard Model (SM) predictions. Of particular interest is the search for nonresonant Higgs boson pair, known as di-Higgs (HH), production. This process has a strong dependence on the Higgs self-coupling, which is a key ingredient of the electroweak symmetry breaking mechanism and a sensitive probe for physics beyond the SM (BSM physics) in various scenarios, such as two-Higgs-doublet models [5], composite Higgs models [6], twin Higgs models [7], and the minimal supersymmetric extension of the SM [8, 9]. The Higgs self-coupling also plays a fundamental role in understanding the stability of the universe [10].

The dominant SM HH production process is gluon–gluon fusion (ggF). Its cross-section, for a Higgs boson mass $m_H = 125$ GeV, calculated at next-to-next-to-leading order (NNLO) including finite top-quark-mass effects [11], is 31.05 fb at a center-of-mass energy $\sqrt{s} = 13$ TeV. The two dominant leading-order Feynman diagrams contributing to this process are shown in Figure 1, where Figure 1(a) is commonly referred to as the *box* diagram and Figure 1(b) as the *triangle* diagram. The triangle diagram introduces the dependence on the trilinear Higgs self-coupling, λ , shown by the red vertex in Figure 1(b), which can be expressed in terms of its modifier, κ_λ .¹ In the SM, these two diagrams interfere destructively. As a result, the HH production cross-section and kinematic properties depend critically on the value of κ_λ .

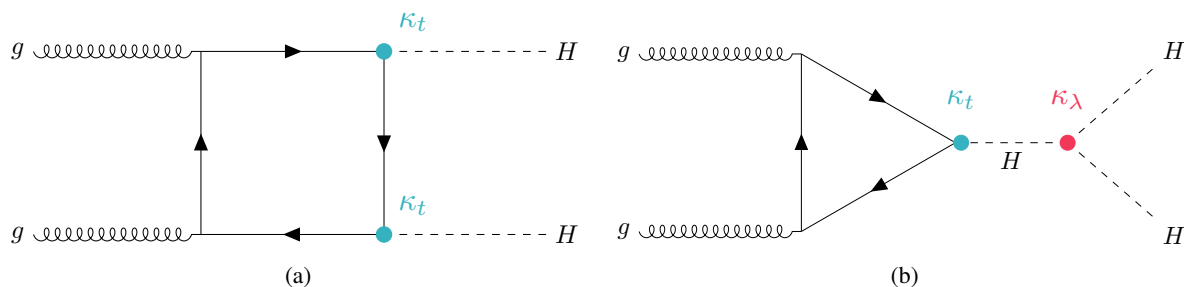


Figure 1: The two leading-order gluon–gluon fusion di-Higgs production Feynman diagrams: (a) the box diagram; (b) the triangle diagram.

The HH production process with the second-highest cross-section in the SM is vector-boson fusion (VBF), with a calculated value of 1.73 fb at next-to-next-to-next-to-leading order (N^3 LO) [12], for $m_H = 125$ GeV at $\sqrt{s} = 13$ TeV. Figure 2 illustrates the Feynman diagrams involved in di-Higgs production via vector-boson fusion at leading order (LO). The coupling modifiers κ_λ , κ_V and κ_{2V} are respectively shown at the HHH , HVV and HHV interaction vertices, where V stands for the gauge vector bosons W or Z . In the SM, the divergences in the Figures 2(b) and 2(c) diagrams exactly cancel out due to perturbative unitarity. As κ_V and κ_{2V} depart from their SM value of one, this canceling out no longer occurs, introducing a linear dependence of the cross-section on the effective center-of-mass energy of the incoming vector bosons [13]. Therefore, the Higgs bosons produced in non-SM κ_V/κ_{2V} scenarios are expected to be more energetic and more central in the detector on average. This increase in the energy of Higgs bosons with increasing deviation from the SM continues up to the scale of some new physics, which is required to unitarize the total amplitude.

¹ A coupling modifier, κ , is defined as the ratio of the modified coupling to its SM value, $\kappa = c/c^{\text{SM}}$. By definition, $\kappa = 1$ denotes the value of the coupling predicted by the SM.

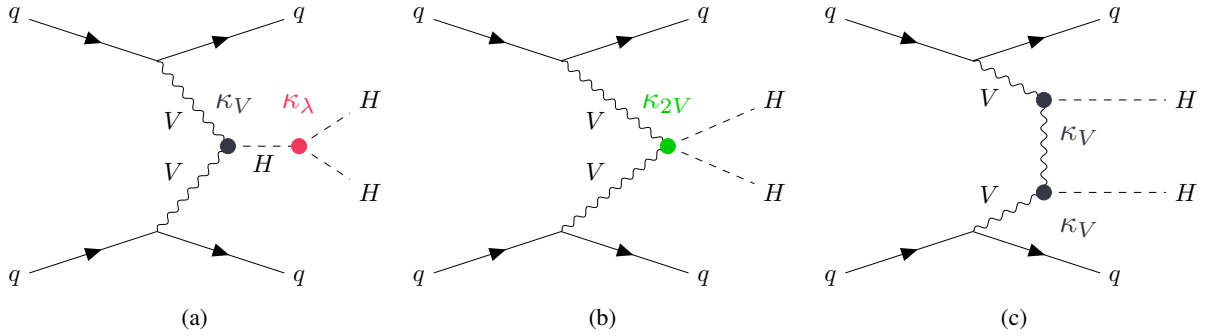


Figure 2: The three tree-level vector-boson fusion di-Higgs production Feynman diagrams.

The analysis described in this paper targets the HH process in the $b\bar{b}b\bar{b}$ final state, in both the ggF and VBF production modes, using the data collected by ATLAS between 2016 and 2018, during Run 2 of the LHC. Assuming the SM branching ratio of 58.2% for $H \rightarrow b\bar{b}$ [14, 15], about one third of di-Higgs events decay into $b\bar{b}b\bar{b}$, making it the most abundant di-Higgs final state. However, as this is a fully hadronic final state, the analysis faces the challenge of large backgrounds, which originate mostly from nonresonant QCD production of multiple heavy (b/t) quarks, as well as from light-quark-initiated jets misidentified as originating from heavy quarks.

The results are interpreted in terms of constraints on the κ_λ and κ_{2V} coupling modifiers, assuming $\kappa_V = 1$. The analysis also provides one- and two-dimensional constraints on relevant couplings in the SM effective field theory (SMEFT) [16–18] and Higgs effective field theory (HEFT) [19, 20] frameworks. In the SMEFT framework, the effects of new physics may be described with an effective Lagrangian:

$$\mathcal{L}_{\text{SMEFT}} = \mathcal{L}_{\text{SM}} + \frac{1}{\Lambda^2} \sum_k c_k^{(6)} O_k^{(6)},$$

where \mathcal{L}_{SM} represents the SM Lagrangian, O_k are higher-dimensional local operators, c_k are the Wilson coefficients, and Λ is the mass scale of the new physics phenomena (set to 1 TeV for this result). The analysis considers operators O_k in the Warsaw basis, which provides a complete set of operators allowed by SM gauge symmetries at dimension six [21] (dimension-five operators introduce lepton and baryon number violation, and are therefore ignored in this result). The five operators relevant to the HH process and their coefficients, c_H , $c_{H\Box}$, c_{tH} , c_{tG} , and c_{HG} , are listed in Table 1 [22]. The computation of amplitudes from the above Lagrangian includes three terms: a pure SM term, a “quadratic” term of order $(1/\Lambda^4)$ including purely new physics, and a “linear” term of order $(1/\Lambda^2)$ accounting for the interference between the SM and new physics. The SMEFT constraints calculated in this analysis include both the linear and quadratic new physics terms.

In the HEFT framework, new physics in the electroweak sector is described through anomalous couplings of the Higgs boson. The organization of the HEFT Lagrangian is guided by chiral perturbation theory [23], with the low-energy dynamics of electroweak symmetry breaking described using a nonlinear realization of the gauge symmetry group $SU(2)_L \times U(1)_Y$. One advantage of the HEFT framework is that the anomalous single-Higgs-boson and HH couplings are defined separately, allowing simplified HH interpretations. In the HEFT Lagrangian, ggF HH production is described at LO by five relevant operators and their associated Wilson coefficients: c_{HHH} , $c_{t\bar{t}H}$, c_{ggH} , c_{ggHH} , and $c_{t\bar{t}HH}$. In this formalism, c_{HHH} is equivalent to κ_λ and $c_{t\bar{t}H}$ is equivalent to the modifier for the coupling between the Higgs boson and top quark, κ_t , shown by the

Table 1: The five relevant SMEFT coefficients and their corresponding dimension-6 operators, as defined in the Warsaw basis [21, 22].

Wilson Coefficient	Operator
c_H	$(H^\dagger H)^3$
$c_{H\Box}$	$(H^\dagger H)\Box(H^\dagger H)$
c_{tH}	$(H^\dagger H)(\bar{Q}\tilde{H}t)$
c_{HG}	$H^\dagger H G_{\mu\nu}^A G_A^{\mu\nu}$
c_{tG}	$(\bar{Q}\sigma^{\mu\nu}T^A t)\tilde{H}G_{\mu\nu}^A$

light blue vertex in Figure 1. Fixing $c_{t\bar{t}H} = c_{HHH} = 1$ and $c_{ggH} = c_{ggHH} = c_{t\bar{t}HH} = 0$ restores the SM. At next-to-leading order (NLO), seven HEFT benchmark models (BM) [24] have been defined using cluster analysis [25] to probe a wide variety of characteristic shapes of the m_{HH} spectrum resulting from different BSM scenarios. The values of the coefficients used to define these scenarios are given in Table 2.

Table 2: The values of the HEFT Wilson coefficients in the SM and in seven BSM benchmark models, as defined in Ref. [24].

Benchmark Model	c_{HHH}	$c_{t\bar{t}H}$	c_{ggH}	c_{ggHH}	$c_{t\bar{t}HH}$
SM	1	1	0	0	0
BM1	3.94	0.94	1/2	1/3	-1/3
BM2	6.84	0.61	0.0	-1/3	1/3
BM3	2.21	1.05	1/2	1/2	-1/3
BM4	2.79	0.61	-1/2	1/6	1/3
BM5	3.95	1.17	1/6	-1/2	-1/3
BM6	5.68	0.83	-1/2	1/3	1/3
BM7	-0.10	0.94	1/6	-1/6	1

The ATLAS Collaboration has previously published search results for nonresonant $HH \rightarrow b\bar{b}b\bar{b}$ production using 27 fb^{-1} of early Run 2 data [26], and a dedicated search for VBF HH production in 126 fb^{-1} of data collected between 2016 and 2018 [27]. The present analysis benefits from the use of the 2016–2018 data for both production channels and also takes advantage of improvements in jet reconstruction and in the identification of jets arising from the decays of b -quarks (“ b -tagging”) achieved by the ATLAS Collaboration since the publication of Ref. [26]. In addition, the analysis employs a fully data-driven technique for the background estimation, which uses an artificial neural network to perform a kinematic reweighting of data from an alternative phase space to model the background in the region of interest. The CMS Collaboration has also published results of a search for nonresonant $HH \rightarrow b\bar{b}b\bar{b}$ with its full Run 2 dataset [28], setting the observed (expected) upper limit on the HH cross-section at 3.9 (7.8) times the SM predicted cross-section, and restricting the allowed interval for κ_λ to $[-2.3, 9.4]$ ($[-5.0, 12.0]$), both at 95% confidence level (CL). A more recent CMS $HH \rightarrow b\bar{b}b\bar{b}$ publication [29], in which the analysis exploits topologies arising from highly energetic Higgs boson decays into $b\bar{b}$, sets the observed (expected) upper limit at 9.9 (5.1) times the SM cross-section expectation, and restricts the allowed interval for κ_{2V} to $[0.62, 1.41]$ ($[0.66, 1.37]$), at 95% CL. Other searches for nonresonant HH production were performed by ATLAS and CMS in the $b\bar{b}\tau^+\tau^-$ [30, 31], $b\bar{b}\gamma\gamma$ [32, 33], $b\bar{b}\ell^+\nu\ell^-\nu$ [34, 35] decay channels, as well as by

ATLAS in the $b\bar{b}qql\nu$ [36], $WW^*\gamma\gamma$ [37] and WW^*WW^* [38] decay channels. Amongst them, the most sensitive results to date from ATLAS come from the $b\bar{b}\gamma\gamma$ analysis, which sets the observed (expected) 95% CL upper limit on the SM nonresonant HH cross-section at 4.2 (5.7) times the SM expectation and restricts the corresponding κ_λ interval to $[-1.5, 6.7]$ ($[-2.4, 7.7]$). The most sensitive results to date from CMS come from the combination of the $b\bar{b}ZZ$, multilepton, $b\bar{b}\gamma\gamma$, $b\bar{b}\tau\tau$, and $b\bar{b}b\bar{b}$ analyses, which set the observed (expected) 95% CL upper limit on the SM nonresonant HH cross-section at 3.4 (2.5) times the SM expectation and restricts the corresponding observed κ_λ interval to $[-1.24, 6.49]$ [39].

This document is structured as follows. The ATLAS detector and the data and simulated events used in the analysis are described in Sections 2 and 3, respectively. Section 4 presents the reconstruction and identification of physics objects in this analysis and Section 5 details the event selection and categorization. The background modeling method is described in Section 6, the systematic uncertainties are detailed in Section 7 and, finally, the results are reported in Section 8 and the conclusion is given in Section 9.

2 ATLAS detector

The ATLAS detector [40] at the LHC covers nearly the entire solid angle around the collision point.² It consists of an inner tracking detector surrounded by a thin superconducting solenoid, electromagnetic and hadron calorimeters, and a muon spectrometer incorporating three large superconducting air-core toroidal magnets.

The inner-detector (ID) system is immersed in a 2 T axial magnetic field and provides charged-particle tracking in the range $|\eta| < 2.5$. The high-granularity silicon pixel detector covers the vertex region and typically provides four space-point measurements per track, the first hit normally being in the insertable B-layer installed before Run 2 [41, 42]. Following the pixel detector is the silicon microstrip tracker, which usually provides eight measurements per track. These silicon detectors are surrounded by the transition radiation tracker, which enables radially extended track reconstruction up to $|\eta| = 2.0$.

The calorimeter system covers the pseudorapidity range $|\eta| < 4.9$. Within $|\eta| < 3.2$, electromagnetic calorimetry is provided by barrel and endcap high-granularity lead/liquid-argon (LAr) calorimeters, with an additional thin LAr presampler covering $|\eta| < 1.8$ to correct for energy loss in material upstream of the calorimeters. Hadron calorimetry is provided by the steel/scintillator-tile calorimeter, segmented into three barrel structures within $|\eta| < 1.7$, and two copper/LAr hadron endcap calorimeters. The solid angle coverage is completed with forward copper/LAr and tungsten/LAr calorimeter modules optimized for electromagnetic and hadronic energy measurements respectively.

The muon spectrometer (MS) comprises separate trigger and high-precision tracking chambers measuring the deflection of muons in a magnetic field generated by the superconducting air-core toroidal magnets. The field integral of the toroids ranges between 2.0 and 6.0 T-m across most of the detector. A set of precision chambers covers the region $|\eta| < 2.7$ with three layers of monitored drift tubes, complemented by cathode-strip chambers in the forward region, where the background is highest. The muon trigger system

² ATLAS uses a right-handed coordinate system with its origin at the nominal interaction point (IP) in the center of the detector and the z -axis along the beam pipe. The x -axis points from the IP to the center of the LHC ring, and the y -axis points upwards. Cylindrical coordinates (r, ϕ) are used in the transverse plane, ϕ being the azimuthal angle around the z -axis. The pseudorapidity is defined in terms of the polar angle θ as $\eta = -\ln \tan(\theta/2)$. Angular distance is measured in units of $\Delta R \equiv \sqrt{(\Delta\eta)^2 + (\Delta\phi)^2}$.

covers the range $|\eta| < 2.4$ with resistive-plate chambers in the barrel, and thin-gap chambers in the endcap regions.

Interesting events are selected by the first-level trigger system implemented in custom hardware, followed by selections made by algorithms implemented in software in the high-level trigger [43]. The first-level trigger accepts events from the 40 MHz bunch crossings at a rate below 100 kHz, which the high-level trigger reduces in order to record events to disk at about 1 kHz.

An extensive software suite [44] is used in data simulation, in the reconstruction and analysis of real and simulated data, in detector operations, and in the trigger and data acquisition systems of the experiment.

3 Data and simulated samples

3.1 Data sample

This analysis is performed in LHC proton–proton (pp) collision data at $\sqrt{s} = 13$ TeV collected between 2016 and 2018. Only data collected during stable beam conditions are used, with all relevant detector systems functional [45], corresponding to an integrated luminosity of 126 fb^{-1} . During 2016 data taking, a fraction of the data (8.3 fb^{-1}) was affected by an inefficiency in the online primary vertex reconstruction, which reduced the efficiency of the b -tagging algorithms in the trigger; those events were not retained for further analysis, resulting in an integrated luminosity of 24.6 fb^{-1} for the 2016 dataset. The integrated luminosities of the 2017 and 2018 datasets are 43.7 fb^{-1} and 57.7 fb^{-1} , respectively.

The analysis uses events that satisfy either of two types of trigger signatures, each with different requirements on the number of jets and their b -tagging status [46]. The jets used are reconstructed with the anti- k_r algorithm [47, 48], with a radius parameter of $R = 0.4$. The b -tagging is performed at the trigger level with the MV2c20 algorithm in 2016 and the MV2c10 algorithm in 2017 and 2018 [46], with a range of b -jet identification efficiency operating points from 40% to 70% (as calculated from simulated $t\bar{t}$ samples.) The first of the two trigger signatures used for selecting $b\bar{b}b\bar{b}$ events requires two b -jets plus one additional jet (“ $2b1j$ ”), while the second requires two b -jets plus two additional jets (“ $2b2j$ ”). The minimum transverse energy (E_T) requirement on the jets is 35 GeV for all jets used in the $2b2j$ trigger. In the $2b1j$ trigger, the b -tagged jets must have $E_T > 55$ GeV, while the requirement on the minimum E_T of the additional jet is between 100 and 150 GeV, depending on the year of data taking.

3.2 Simulated samples

Monte Carlo (MC) simulation is used for the modeling of signal events, as well as to produce event samples of background processes for cross-checks and validation studies. The Higgs boson mass is set to 125 GeV in the simulation. All samples were processed by the ATLAS simulation framework [49] and the detector response was simulated with GEANT4 [50].

The ggF signal process was simulated using the POWHEG BOX v2 generator [51–53] at NLO, including finite top-quark-mass effects, using the PDF4LHC15 [54] parton distribution function (PDF) set. Parton showers and hadronization were simulated with PYTHIA 8.244 [55] with the A14 set of tuned parameters [56] and the NNPDF2.3LO PDF set [57]. The SM ggF HH cross-section was taken as $\sigma_{\text{ggF}} = 31.05 \text{ fb}$, calculated at NNLO including finite top-quark-mass effects [11]. Signal samples for the ggF process were generated

explicitly for coupling modifier values of $\kappa_\lambda = 1$ and 10. A reweighting method is used to obtain a ggF signal sample at each κ_λ value, as described in Ref. [58]: scale factors are derived as a function of κ_λ in bins of the generator-level invariant mass of the HH system by performing a linear combination of generator-level samples at three different κ_λ values ($\kappa_\lambda = 0, 1, \text{ and } 20$). The $\kappa_\lambda = 10$ ggF signal sample is used to validate the derived scale factors; this generated sample and the signal sample obtained from the reweighting method are found to agree within the statistical precision of the simulated sample. Additional generator-level ggF HH signal samples without parton showering were produced with POWHEG BOX v2 for the $\kappa_\lambda = 0$ and 20 coupling modifier configurations to provide a basis for the κ_λ reweighting, along with the SM ggF sample. For the reweighted ggF signal, the NNLO cross-section as a function of κ_λ is taken from Ref. [11]. In order to assess parton showering uncertainties, alternative ggF samples were generated using the POWHEG BOX v2 generator at NLO with the PDF4LHC15 PDF set, interfaced to HERWIG 7.1.6 [59] for parton showering and hadronization using the HERWIG 7.1-default set of tuned parameters [60] and MMHT2014LO PDF set [61].

To extract SMEFT coefficient constraints, parton-level ggF HH samples were generated with MADGRAPH5_AMC@NLO [62–64] with the SMEFT@NLO model [65] for a variety of SMEFT coefficients. A finely spaced multidimensional grid of signal samples was obtained using a LO-derived reweighting procedure in the generator-level invariant mass of the HH system; this procedure is similar to that used to obtain κ_λ variations for the ggF signal, as described above. To extract HEFT coefficient constraints, a similar NLO-derived reweighting procedure was applied to the simulated reconstruction-level ggF signal sample to produce a variety of HEFT signal scenarios, including the seven benchmark scenarios defined in Section 1, following the prescription outlined in Refs. [66, 67]. Additional K -factors were applied to the SMEFT samples; these K -factors were derived using the ratio of the NLO cross-section to the LO cross-section at the equivalent HEFT point, as obtained using the HEFT to SMEFT translation from Ref. [24].³

The VBF signal process was simulated using MADGRAPH 2.7.3 [63] at LO with the NNPDF3.0NLO PDF set [68], interfaced with PYTHIA 8.244 for parton showering and hadronization using the A14 set of tuned parameters and NNPDF2.3LO PDF set. Signal samples for the VBF process were generated explicitly for coupling modifier values of $(\kappa_\lambda, \kappa_{2V}, \kappa_V) = (1, 1, 1), (1, 1.5, 1), (2, 1, 1), (10, 1, 1), (1, 1, 0.5), (-5, 1, 0.5), (0, 1, 1), (1, 0, 1), \text{ and } (1, 3, 1)$. A linear combination of the first six of the listed samples is used to derive distributions for a finer granularity of κ_{2V} values, following a technique used previously to generate κ_λ distributions [69]. The specific basis of six samples utilized is chosen to avoid large statistical uncertainties in the reweighted signal samples resulting from sparsely populated areas of kinematic phase space. The generated VBF signal samples not included in the linear combination basis – $(\kappa_\lambda, \kappa_{2V}, \kappa_V) = (0, 1, 1), (1, 0, 1), \text{ and } (1, 3, 1)$ – were used to validate the performance of the combination method. These generated samples and the corresponding signal samples obtained from the combination method were found to agree within the statistical precision of the simulated samples. The cross-section for the VBF HH process, evaluated at $N^3\text{LO}$ in QCD, is 1.73 fb in the SM [12, 70–72]. For the reweighted VBF signal points, the $N^3\text{LO}$ to LO cross-section ratio at the SM value is calculated, and this factor is applied to the cross-sections at each $\kappa_\lambda, \kappa_{2V}, \text{ and } \kappa_V$ point. In order to assess parton showering uncertainties, alternative LO samples were generated using MADGRAPH 2.7.3 with the NNPDF3.0NLO PDF set, interfaced to HERWIG 7.0.4 with the HERWIG 7.1-default set of tuned parameters and MMHT2014LO PDF set for parton showering and hadronization.

Top-quark pair production ($t\bar{t}$) and multijet background processes were simulated in order to validate the

³ Variations in the c_{tG} Wilson coefficient were neglected when calculating K -factors because the corresponding chromomagnetic operator does not appear at LO within HEFT.

background modeling procedure. The $t\bar{t}$ sample was simulated at NLO in α_s using POWHEG BOX v2 [73]. Parton showering, hadronization, and the underlying event were modeled using PYTHIA 8.230. The matrix element calculation uses NNPDF3.0_{NLO} as the PDF set, while the parton shower and underlying-event modeling uses NNPDF2.3_{LO} and the A14 set of tuned parameters. The damping parameter h_{damp} , which effectively regulates radiation at high p_T , was set to 1.5 times the top quark’s mass. The $t\bar{t}$ simulation is normalized using the value of the inclusive cross-section calculated with TOP++ 2.0 [74, 75]. This accounts for NNLO corrections in α_s , including next-to-next-to-leading logarithmic (NNLL) resummation of soft gluon terms. The multijet background samples were modeled using PYTHIA 8.235. This simulates pure QCD 2-to-2 interactions at LO in α_s . Events were showered using the parton shower native to PYTHIA, which includes radiation and splitting that can result in additional jets. The A14 set of tuned parameters and the NNPDF2.3_{LO} PDF set were used.

Other background processes, such as SM Higgs boson, HH (in other final states) and electroweak diboson production, have been estimated to give negligible contributions to the selected event yields and are therefore not included.

The effect of multiple interactions in the same and neighboring bunch crossings (pileup) was modeled by overlaying each simulated hard-scattering event with inelastic pp events generated with PYTHIA 8.186 using the NNPDF2.3_{LO} PDF set and the A3 set of tuned parameters [76]. Additionally, for all HH signal samples, heavy-flavor decays were modeled using EVTGEN 1.7.0 [77].

4 Object reconstruction

Primary vertices from pp interactions are reconstructed [78] using at least two charged-particle tracks with transverse momentum (p_T) above 500 MeV measured with the ID. The vertex with the largest sum of squared track momenta ($\sum p_T^2$) is taken as the hard-scatter primary vertex.

Hadronic jets are reconstructed using the anti- k_t algorithm with radius parameter $R = 0.4$. The jet clustering uses particle-flow objects as inputs [79]. Particle-flow objects are charged-particle tracks matched to the hard-scatter vertex and calorimeter energy clusters after applying an energy subtraction algorithm that removes the calorimeter deposits associated with good-quality tracks from any vertex. The tracking information helps to improve the energy resolution of the calorimeter clusters and reduce the impact from pileup. The momenta of reconstructed jets are calibrated in a multistep procedure [80]. Jets with $p_T < 60$ GeV and $|\eta| < 2.4$ must also satisfy a requirement based on the output of the multivariate “jet vertex tagger” (JVT) algorithm [81], which is used to identify and reject jets in which much of the energy originates from pileup interactions. Correction factors are applied to the simulated events to compensate for differences between the JVT efficiencies in data and simulation. In the $HH \rightarrow b\bar{b}b\bar{b}$ analysis, jets are discarded if they fail the “Tight” JVT working point, corresponding to an average efficiency of 96% for jets from the hard-scatter vertex.

Jets with radius parameter $R = 0.4$ are also reconstructed from topological clusters of energy deposits in the calorimeter [82] and calibrated in the same way as the jets reconstructed from particle-flow objects. These jets are used exclusively for the purpose of applying quality criteria to identify events which are consistent with noise in the calorimeter or noncollision background [83]. Events containing at least one such jet with $p_T > 20$ GeV, satisfying the JVT requirement, but not these quality criteria, are rejected.

The identification of jets originating from b -quarks is performed by the DL1r algorithm [84], which is applied to all jets with $|\eta| < 2.5$. DL1r is based on a multivariate classification technique combining

information from the impact parameters of ID tracks, the presence of displaced secondary vertices, and the reconstructed flight paths of b - and c -hadrons inside the jet. The DL1r working point used in the $HH \rightarrow b\bar{b}b\bar{b}$ analysis is the one that gives 77% efficiency for jets associated with true b -hadrons in simulated $t\bar{t}$ events. At this working point, the light-jet (charm-jet) rejection measured in $t\bar{t}$ simulation is about a factor of 130 (4.9). The calibration of the DL1r algorithm is performed separately for each jet type [85, 86] and correction factors are derived and applied to the simulated samples to compensate for differences between the b -tagging efficiencies in data and simulation.

Muons are reconstructed by matching ID tracks with either MS tracks or aligned individual hits in the MS and performing a combined track fit [87]. They are required to have $p_T > 4 \text{ GeV}$ and $|\eta| < 2.5$, and to satisfy “Medium” identification criteria based on track-quality variables. Muons are used only to apply energy corrections to jets.

A momentum correction is applied to b -tagged jets to account for energy lost to soft out-of-cone radiation and to muons and neutrinos in semileptonic b -hadron decays. This correction follows the procedure used in Ref. [88] and consists of two steps. First, a search is performed for muons located near the jet which fall within a cone of variable size $\Delta R(\mu, \text{jet}) < \min(0.4, 0.04 + 10/p_T^\mu \text{ GeV})$ around the jet axis. If a muon is found, its four-momentum is added to that of the jet, and the energy deposited in the calorimeter by the muon is subtracted from the jet to avoid double counting; this is computed according to the description in Ref. [89]. In the second step, a global scale factor is applied to each b -tagged jet according to its p_T and whether or not it has a muon associated with it. These scale factors are derived from simulation.

5 Analysis selection and categorization

The analysis utilizes a set of criteria to select $HH \rightarrow b\bar{b}b\bar{b}$ candidate events, including dedicated requirements to separate events into orthogonal ggF and VBF signal regions. “Forward” and “central” jets are used with the following selection criteria:

- central jets: $|\eta| < 2.5$ and $p_T > 40 \text{ GeV}$;
- forward jets: $2.5 < |\eta| < 4.5$ and $p_T > 30 \text{ GeV}$.

An initial “preselection” is applied to all events, which requires at least four central jets with $p_T > 40 \text{ GeV}$, at least two of which are b -tagged. As described in Section 3, the events considered in this analysis are selected online through the $2b2j$ or $2b1j$ trigger signatures. In order to simplify the modeling of trigger efficiencies, a further selection is applied using offline kinematic quantities. Events are selected if they have a leading⁴ jet with $p_T > 170 \text{ GeV}$, a third leading jet with $p_T > 70 \text{ GeV}$, and pass the $2b1j$ trigger, or if they fail either of the two jet- p_T requirements and pass the $2b2j$ trigger. This selection step leads to about a 10% loss of signal efficiency, but enables the reliable calculation of simulation-to-data correction factors for estimating the trigger efficiency in the remaining $HH \rightarrow b\bar{b}b\bar{b}$ signal events, depending on which of the above two *trigger classes* they belong to.

Events passing the above preselection are required to contain at least four central jets passing the b -tagging requirement outlined in Section 4. The four highest- p_T b -tagged jets are chosen to reconstruct the decays of the two Higgs bosons. In about 75% of simulated signal events reaching this selection stage, these four jets can be matched one-to-one (within $\Delta R < 0.3$) to the four b -quarks from the decays of the Higgs bosons.

⁴ In this document, terms like “leading”, “subleading” etc for physics objects refer to the ordering of these objects in decreasing p_T .

In signal events where this matching fails, one of the b -quarks from the Higgs boson decays typically produces a jet that is outside the analysis acceptance.

From the four selected b -tagged jets, there are three possible combinatorial pairings to form the two Higgs boson candidates. Of those three configurations, the analysis selects the one in which the higher- p_T jet pair has the smallest ΔR separation. In the simulated samples with SM coupling values, for which the analysis was mainly optimized, this method gives the correct pairing in around 90% of those signal events in which the four b -tagged jets are correctly matched to the b -quarks from the decays of the Higgs bosons. While the pairing accuracy drops for values of the coupling modifiers κ_λ and κ_{2V} that result in softer p_T spectra for the produced Higgs bosons, this pairing method leads to a smoothly varying distribution of the expected background in the plane of the invariant masses of the two Higgs boson candidates, which facilitates the data-driven background estimation described in Section 6.

Events are then subjected to additional selections designed to separate out those consistent with the VBF production mode. For this, events must contain at least two additional jets, central or forward; b -tagged jets are excluded. The two jets forming the pair with the largest invariant mass (m_{jj}) are chosen as the ‘‘VBF jets’’. The VBF jet pair is required to satisfy $m_{jj} > 1$ TeV, and the pseudorapidity separation between the two jets, $|\Delta\eta_{jj}|$, must satisfy $|\Delta\eta_{jj}| > 3$. Lastly, the transverse component of the momentum vector sum of the two VBF jets and the four jets forming the Higgs boson candidates is required to be less than 65 GeV. Events satisfying the above criteria enter the VBF signal region, while those failing to satisfy any of these criteria are considered further in the ggF signal region.

Events satisfying either the ggF or VBF selections are required to satisfy additional selection criteria designed to reduce the background and improve the analysis sensitivity. In order to suppress the $t\bar{t}$ background, a top-veto discriminant X_{Wt} is defined as:

$$X_{Wt} = \min \left[\sqrt{\left(\frac{m_{jj} - m_W}{0.1m_{jj}} \right)^2 + \left(\frac{m_{jjb} - m_t}{0.1m_{jjb}} \right)^2} \right],$$

where $m_W = 80.4$ GeV and $m_t = 172.5$ GeV are the nominal W boson and top quark masses, and m_{jj} and m_{jjb} are the invariant masses of W boson and top quark candidates formed from jet combinations in each event. The ‘‘minimum’’ refers to the minimum value from all possible jet combinations (of one b -tagged jet and two additional untagged jets) that would give a W boson candidate and a corresponding top candidate. The factor of 0.1 in the denominators is chosen to approximate the experimental dijet mass resolution. The W boson candidates are formed from any pair of central jets in the event and the top quark candidates are then reconstructed by pairing the W boson candidates with any remaining b -tagged Higgs boson candidate jets. The X_{Wt} discriminant is designed to quantify the likelihood that an event contains a hadronic top quark decay. Events with $X_{Wt} < 1.5$ are rejected. This reduces the $t\bar{t}$ background by a factor of about 2 in simulated events, for a small loss of signal efficiency, of around 15%, and a similar reduction in the non- $t\bar{t}$, multijet background.

In order to further reduce the overall background contamination, events in the ggF signal region are also required to have reconstructed Higgs bosons that satisfy a pseudorapidity separation $|\Delta\eta_{HH}| < 1.5$. No such requirement is imposed in the VBF signal region, since SM VBF HH signal events tend to have a larger $|\Delta\eta_{HH}|$.

A final analysis selection criterion to test the compatibility of events with the HH decay is applied in both the ggF and VBF selections. A discriminant X_{HH} is defined as:

$$X_{HH} = \sqrt{\left(\frac{m_{H1} - 124 \text{ GeV}}{0.1 m_{H1}}\right)^2 + \left(\frac{m_{H2} - 117 \text{ GeV}}{0.1 m_{H2}}\right)^2},$$

where m_{H1} and m_{H2} are the masses of the leading and subleading reconstructed Higgs boson candidates respectively. The values of 124 GeV and 117 GeV in the X_{HH} definition are chosen in accord with the centers of the m_{H1} and m_{H2} distributions for correctly paired signal events from simulation. Events are required to have $X_{HH} < 1.6$ to be included in the *Signal Region* (SR) of the analysis.

Both the ggF and VBF signal regions are subdivided into a number of orthogonal categories in order to better isolate the HH signal and improve the analysis sensitivity. The X_{HH} and $|\Delta\eta_{HH}|$ quantities are used to define six orthogonal ggF categories. The categories are defined by two intervals in X_{HH} , with boundaries at 0, 0.95, and 1.6, and three in $|\Delta\eta_{HH}|$, with boundaries at 0, 0.5, 1, and 1.5. In the VBF signal region, two categories are defined using the $|\Delta\eta_{HH}|$ quantity, with the dividing boundary at $|\Delta\eta_{HH}| = 1.5$. The $|\Delta\eta_{HH}| < 1.5$ category is more sensitive to VBF signals with non-SM couplings, while the $|\Delta\eta_{HH}| > 1.5$ category is more sensitive to SM VBF production.

The reconstructed invariant mass of the Higgs boson candidate pair, m_{HH} , is used as the discriminating variable for all analysis regions and categories when extracting results, as detailed in Section 8. The m_{HH} distribution is found to have significant separation power between background and signal, for all the different values of coupling modifiers. The binning of the m_{HH} distributions may vary between categories and is chosen in order to both maintain discrimination power and limit the expected statistical uncertainty in each bin to less than approximately 30%. This 30% limit ensures that the assumptions used in the statistical procedure, outlined in Section 8, are satisfied. In the VBF signal region, only events with $m_{HH} > 400$ GeV are considered, as the background in the lower m_{HH} region was found to be inadequately modeled by the data-driven method described in Section 6 when applied to the $3b1f$ control data sample (also described in Section 6). For the ggF signal region, no requirements on m_{HH} are applied.

All the selection steps of the analysis are summarized in Figure 3. The yields in the data and the simulated signal samples for some typical coupling values are shown in Table 3. This sample of data events is referred to as $4b$ events hereafter.

6 Background modeling

After the selection described above, about 90% of the background events come from multijet processes (excluding top quark production), with the approximately 10% remainder almost entirely composed of $t\bar{t}$ events. This background composition was determined by applying the full event selection to simulated samples of the various processes and comparing the yields with the total background estimate in the SR; it is purely meant to be indicative and is not used for deriving any results. The background is modeled using the fully data-driven technique described below.

The background estimation makes use of an alternative set of events, which pass the same b -jet triggers and satisfy all the same selection criteria as the $4b$ events, with one difference: they are required to contain exactly two b -tagged jets. This sample, referred to hereafter as “ $2b$ ”, has about two orders of magnitude more events than the $4b$ sample, hence the presence of any $HH \rightarrow b\bar{b}b\bar{b}$ signal in it is negligible, making it

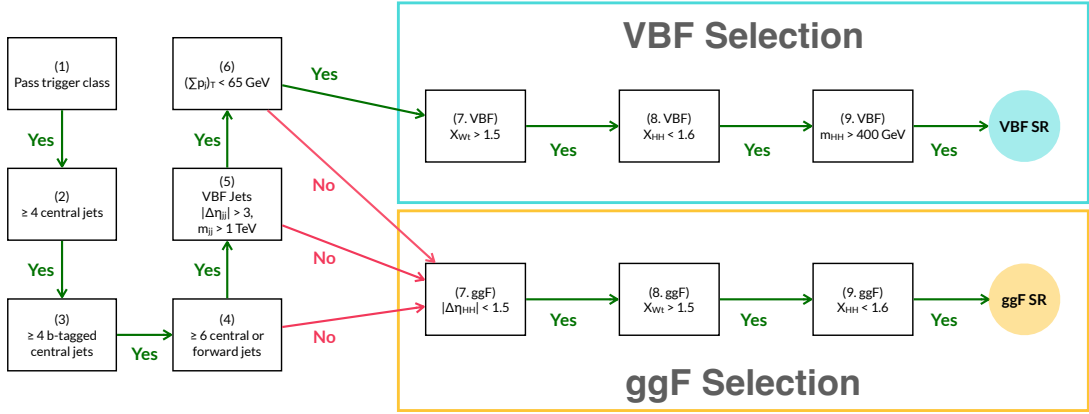


Figure 3: A flowchart summarizing the nine selection criteria used for the VBF and ggF analysis selections. Events must satisfy selection criteria 1–3 in order to be considered for either analysis signal region. Events failing to satisfy any of the selection criteria 4–6 are considered for inclusion in the ggF signal region, while those satisfying selection criteria 4–6 are considered for the VBF signal region.

Table 3: The yields of data and various example ggF and VBF HH signal models at each step of the analysis selection. The “Preselection” entry denotes an initial selection requiring at least four jets with $p_T > 40$ GeV, at least two of which are b -tagged. Events which satisfy the “VBF selection” requirements are considered as part of the VBF signal region of the analysis, while the rest are considered for the ggF signal region. The signal yields are taken from simulation and are normalized by their theoretical cross-sections and the integrated luminosity of 126 fb^{-1} . Corrections for differences in the b -tagging efficiency and trigger acceptance between data and simulation are applied starting from the “Trigger class” requirement.

	Data	ggF Signal		VBF Signal	
		SM	$\kappa_\lambda = 10$	SM	$\kappa_{2V} = 0$
Common preselection					
Preselection	5.70×10^8	530	7300	22	630
Trigger class	2.49×10^8	380	5300	16	410
ggF selection					
Fail VBF selection	2.46×10^8	380	5200	14	330
At least 4 b -tagged central jets	1.89×10^6	86	1000	1.9	65
$ \Delta\eta_{HH} < 1.5$	1.03×10^6	72	850	0.94	46
$X_{Wt} > 1.5$	7.51×10^5	60	570	0.74	43
$X_{HH} < 1.6$ (ggF signal region)	1.62×10^4	29	180	0.24	23
VBF selection					
Pass VBF selection	3.30×10^6	5.2	81	2.2	71
At least 4 b -tagged central jets	2.71×10^4	1.1	15	0.74	28
$X_{Wt} > 1.5$	2.18×10^4	1.0	11	0.67	26
$X_{HH} < 1.6$	5.02×10^2	0.48	3.1	0.33	17
$m_{HH} > 400$ GeV (VBF signal region)	3.57×10^2	0.43	1.8	0.30	16

suitable for the background estimation. The jets selected to form the two Higgs boson candidates in the $2b$ events are the two b -tagged jets and the two untagged central jets with the highest p_T (excluding the VBF

jets in the VBF categories).

The kinematic properties of the $2b$ and $4b$ events are not expected to be identical, partly due to different processes contributing to the two samples, but also due to differences in the trigger acceptance and because the probability of tagging a b -jet varies as a function of jet p_T and η . Therefore, a reweighting function is required, which, when applied to the $2b$ events, maps their kinematic distributions onto the corresponding $4b$ distributions. This function is derived using the $2b$ and $4b$ events in a *Control Region* (CR) surrounding the SR in the reconstructed (m_{H1}, m_{H2}) plane and then applied to the $2b$ events in the SR to produce the background estimate. The ‘‘inner edge’’ of the CR is defined by $X_{HH} = 1.6$ and the ‘‘outer edge’’ by the circle:

$$R_{\text{CR}} = \sqrt{(m_{H1} - 1.05 \cdot 124 \text{ GeV})^2 + (m_{H2} - 1.05 \cdot 117 \text{ GeV})^2} = 45 \text{ GeV} .$$

The shift of the center of the above circle by a factor of 1.05, relative to $X_{HH} = 0$, is found to be the optimal trade-off between having a good number of events outside of the SR and avoiding the low m_{H1}/m_{H2} regions, where the differences between $2b$ and $4b$ kinematic distributions are larger. The CR is split into four roughly equal directional quadrants, defined by 45° and 135° lines passing through the SR center, (124, 117) GeV. The four quadrants are given labels based on compass directions: the upper quadrant Q_N , the lower Q_S , the left Q_W , and the right Q_E . The above lines also define four quadrants, with the same names as above, in the SR. Events in CR Q_N and Q_S , hereafter referred to as CR1, are used to derive the reweighting function for the nominal background estimate, while an alternative reweighting function, derived from the CR events in Q_E and Q_W (referred to hereafter as CR2) is used to define a systematic uncertainty related to the reweighting function interpolation into the SR, as detailed in Section 7. The boundaries of the SR, CR1, and CR2 in the reconstructed (m_{H1}, m_{H2}) plane are shown in Figure 4. The horizontal and vertical bands of lower event density around 80 GeV visible in these plots are caused by the X_{Wt} selection criterion.

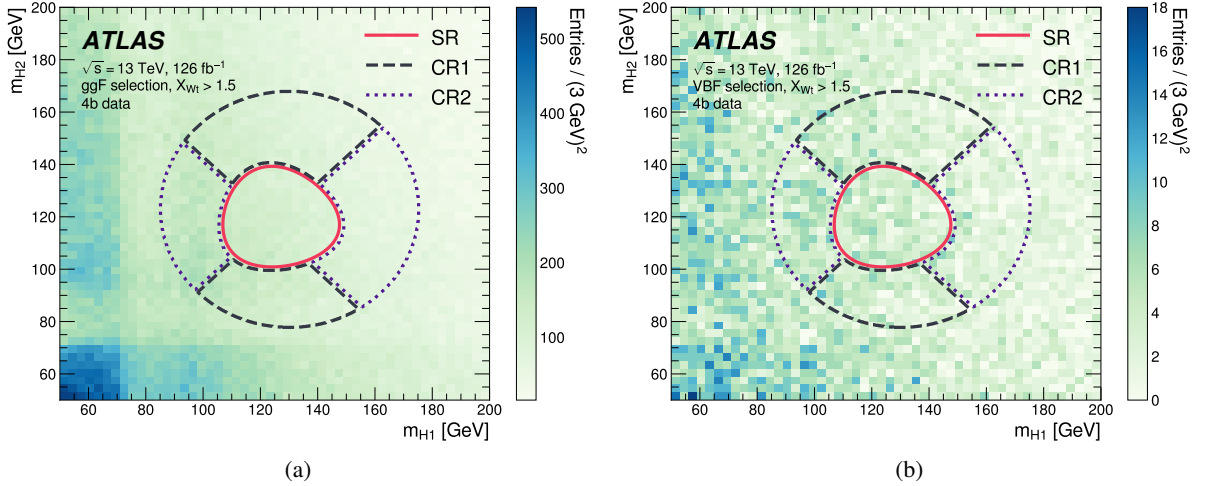


Figure 4: The mass planes of the reconstructed Higgs boson candidates for the (a) ggF and (b) VBF signal regions of the analysis, shown for the $4b$ data events. In (a), the analysis selection up to step 8 (as outlined in Figure 3) of the ggF selection has been applied, while in (b), the analysis selection up to step 7 of the VBF selection has been applied. The continuous red line describes the Signal Region (SR), the dashed line describes Control Region 1 (CR1) and the dotted line describes Control Region 2 (CR2).

The reweighting function has the form:

$$w(\vec{x}) = \frac{p_{4b}(\vec{x})}{p_{2b}(\vec{x})}, \quad (1)$$

where $p_{4b}(\vec{x})$ and $p_{2b}(\vec{x})$ are the probability density functions for $4b$ and $2b$ data, respectively, over a set of kinematic variables \vec{x} . The computation of $w(\vec{x})$ is a density ratio estimation problem, for which a variety of approaches exist. The method employed in this analysis is modified from Refs. [90, 91] and makes use of an artificial neural network (NN). This NN is trained on $2b$ and $4b$ CR1 data (or CR2 data, for determining systematic uncertainties, as described Section 7). The training minimizes the following loss function:

$$\mathcal{L}(w(\vec{x})) = \int d\vec{x} \left[\sqrt{w(\vec{x})} p_{2b}(\vec{x}) + \frac{1}{\sqrt{w(\vec{x})}} p_{4b}(\vec{x}) \right],$$

The function in Eq. (1) minimizes this loss by equalizing the contributions from the two terms. The kinematic variables used to make up \vec{x} are listed in Table 4 for the ggF and VBF signal regions; they are among those kinematic variables that exhibit larger differences between the $2b$ and $4b$ events. The NN used in the ggF signal region has three densely connected hidden layers of 50 nodes, each with a rectified linear unit activation function [92], and a single-node linear output. A similar architecture is chosen for the NN used in the VBF signal region, except that only 20 nodes are used in each of the three hidden layers. This reflects the fact that the $2b$ and $4b$ sample sizes in the VBF signal region are nearly two orders of magnitude smaller than the corresponding ones in the ggF signal region. This is also the reason behind the choice to perform the NN training in the VBF signal region for all data-taking years together, with the year index as a one-hot encoded input feature.⁵ For the ggF signal region, a dedicated reweighting is derived for each year separately, which, thanks to the adequate sample sizes, deals better with the different levels of disparity between $2b$ and $4b$ distributions, due to the differences in the trigger conditions from year to year. Finally, in order to ensure that there are adequate numbers of $4b$ events for both the ggF and VBF NN trainings, these trainings are performed inclusively, before separating the events into the $|\Delta\eta_{HH}|$ categories (the CR events have $X_{HH} > 1.6$, hence it would not be possible to separate them into the X_{HH} categories defined for the SR events). Both $|\Delta\eta_{HH}|$ and X_{HH} are found to be insensitive to the kinematic reweighting, and so the inclusive training is not expected to introduce any additional bias when separating the events into the various categories.

In order to estimate and mitigate the impact of the varying initial conditions and limited size of the training samples on the NN training, the deep ensembles technique [93] is used together with a bootstrap resampling [94] of the training data. This entails constructing a set of training datasets by sampling with replacement from the original dataset. In this analysis, this is approximated by the usage of different random training weights, following a Poisson distribution with $\mu = 1$, for each event in each training. The NN is trained independently on each element of this set, using different initial conditions each time. This results in an ensemble of reweighting functions. Each reweighting function is further multiplied by a normalization factor, such that the number of reweighted $2b$ events is equal to the number of $4b$ events in the region where the NN is trained. In this analysis, the ensembles comprise 100 reweighting functions each, hence 100 weights are calculated for each $2b$ event in the SR. The background estimate uses the mean of these weights for each event, and the variation of the background predictions from the ensemble

⁵ One-hot encoding is a standard technique in machine learning. For example, for the data-taking years in the VBF reweighting, instead of presenting the year numbers as input features to the NN, one-hot encoding uses three input features: (1, 0, 0) for 2016, (0, 1, 0) for 2017, and (0, 0, 1) for 2018.

Table 4: The set of input variables used for the $2b$ to $4b$ reweighting in the ggF and VBF channels respectively.

ggF	VBF
1. $\log(p_T)$ of the 2 nd leading Higgs boson candidate jet	1. Maximum dijet mass from the possible pairings of the four Higgs boson candidate jets
2. $\log(p_T)$ of the 4 th leading Higgs boson candidate jet	2. Minimum dijet mass from the possible pairings of the four Higgs boson candidate jets
3. $\log(\Delta R)$ between the closest two Higgs boson candidate jets	3. Energy of the leading Higgs boson candidate
4. $\log(\Delta R)$ between the other two Higgs boson candidate jets	4. Energy of the subleading Higgs boson candidate
5. Average absolute η value of the Higgs boson candidate jets	5. Second-smallest ΔR between the jets in the leading Higgs boson candidate (from the three possible pairings for the leading Higgs candidate)
6. $\log(p_T)$ of the di-Higgs system	6. Average absolute η value of the four Higgs boson candidate jets
7. ΔR between the two Higgs boson candidates	7. $\log(X_{Wt})$
8. $\Delta\phi$ between jets in the leading Higgs boson candidate	8. Trigger class index as one-hot encoder
9. $\Delta\phi$ between jets in the subleading Higgs boson candidate	9. Year index as one-hot encoder (for years inclusive training)
10. $\log(X_{Wt})$	
11. Number of jets in the event	
12. Trigger class index as one-hot encoder	

of reweighting functions is used to estimate a systematic uncertainty for the stability of the NN training procedure, as described in Section 7.

The effect of the above reweighting procedure in CR1, where the reweighting function is derived, is illustrated in Figure 5 for the m_{HH} distribution of the ggF-selected events and in Figure 6 for the X_{Wt} distribution of the VBF-selected events. The reweighted “ $2b$ ” distributions agree with the corresponding “ $4b$ ” distributions to within about 10% for most of the phase space, with some larger deviations observed in bins near the tails of the distributions where fewer data events are available. A large number of additional kinematic variables were also studied before and after applying the reweighting in order to validate the performance of the NN. For all variables, the level of agreement, as quantified by the χ^2 metric, either improves after the reweighting or, for variables where the “ $2b$ ” and “ $4b$ ” distributions are already similar, changes only slightly.

The background modeling procedure was tested and found to produce good results in a large simulated $t\bar{t}$ sample and a much smaller sample of simulated (non- $t\bar{t}$) multijet events in the SR. The procedure was also tested in several control data samples orthogonal to the nominal event selection, where the presence of any HH signal is negligible and the $4b$ events in the corresponding SR can be compared with the reweighted SR $2b$ events without any bias. These samples, summarized in Table 5, include: (a) events satisfying all the $2b/4b$ ggF selection criteria, with the difference that the $|\Delta\eta_{HH}| < 1.5$ cut is inverted; (b) events satisfying all the $2b/4b$ selection criteria, except that the center of the SR (and hence also of CR1 and CR2) is shifted, to avoid any overlap with the nominal SR; and (c) events that satisfy all the same $4b$ selection criteria, except that, in terms of b -tagging, they contain exactly three b -tagged jets, and the fourth jet is taken as the highest- p_T jet that fails a looser working point of the b -tagging algorithm (one that gives 85%

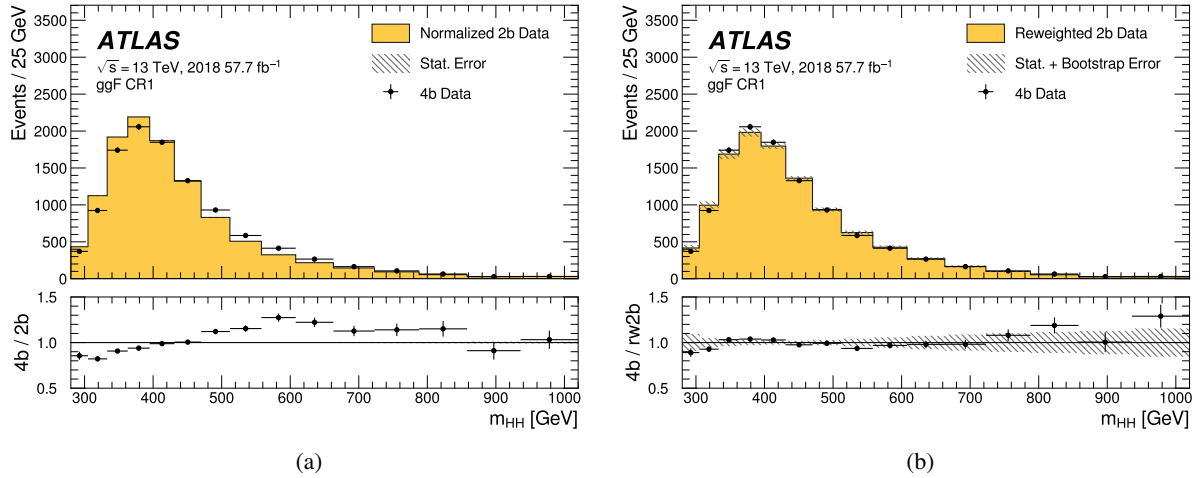


Figure 5: Comparison of the $2b$ (yellow histogram with hatching) and $4b$ (black points with error bars) m_{HH} distributions, for events in Control Region 1 (CR1) of the ggF signal region from the 2018 data: (a) before the kinematic reweighting of the $2b$ events, with only a normalization factor applied; and (b) after the kinematic reweighting of the $2b$ events. The error bars indicate the statistical uncertainty of the $4b$ data, while the hatching indicates the statistical uncertainty of the $2b$ data. The latter is only the Poisson uncertainty of the $2b$ data, in (a), while in (b), it also includes the uncertainty from the bootstrap procedure described in Section 7. The hatching in (a) is narrower than the line width of the plotted histogram.

efficiency for b -jets in simulated $t\bar{t}$ events). This sample, hereafter referred to as $3b1f$, has about one order of magnitude more events than the $4b$ sample and a negligible amount of HH signal; hence it is used to derive a nonclosure systematic uncertainty for the reweighting procedure, as discussed in Section 7. No significant background modeling nonclosure was observed in the other control data samples.

7 Systematic uncertainties

The uncertainties with the greatest impact on the analysis sensitivity are those arising from the data-driven background estimate described in Section 6. These uncertainties have two main sources: the limited sample sizes in the CR and SR, and physical differences between the CR, where the $2b$ reweighting function is derived, and the SR, where it is applied.

As described in Section 6, the ensemble of 100 reweighting functions results in 100 separate background predictions. An m_{HH} histogram can be constructed from each of these predictions, and the standard deviation of the predictions in each bin is taken as the bootstrap uncertainty. The uncertainty is treated as uncorrelated across m_{HH} bins.

An additional statistical uncertainty results from the limited sample size of the $2b$ SR dataset in which the trained background reweighting network is applied to obtain the final background estimate. A Poisson uncertainty is taken for each m_{HH} bin, which is combined in quadrature with the bootstrap uncertainty described above.

For the background estimate, the uncertainty component related to the kinematic differences between the SR and CR1 is evaluated by using alternative predictions from the CR2 region. Four alternative

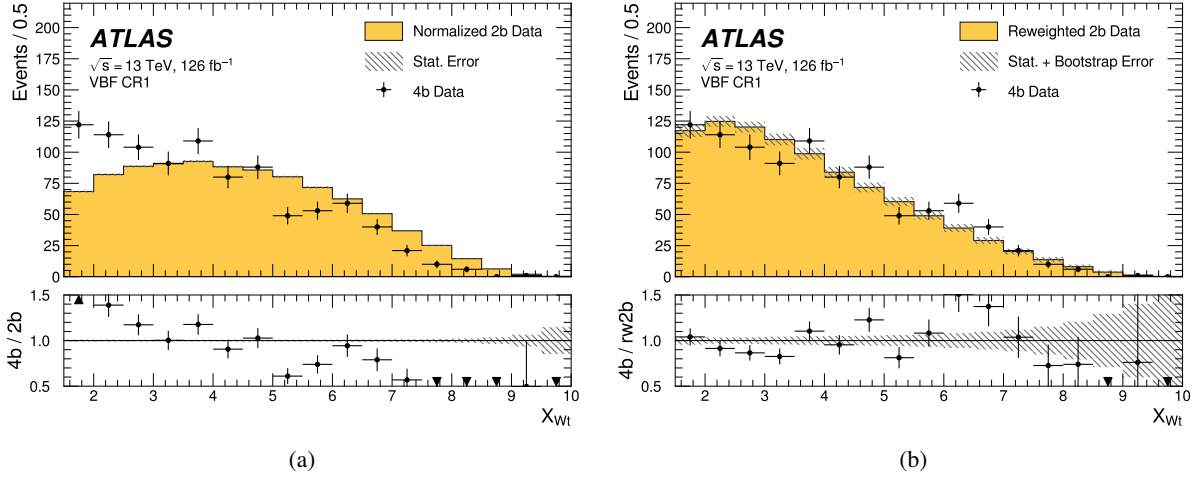


Figure 6: Comparison of the $2b$ (yellow histogram with hatching) and $4b$ (black points with error bars) X_{Wt} distributions, for events in Control Region 1 (CR1) of the VBF signal region: (a) before the kinematic reweighting of the $2b$ events, with only a normalization factor applied; and (b) after the kinematic reweighting of the $2b$ events. The error bars indicate the statistical uncertainty on the $4b$ data, while the hatching indicates the statistical uncertainty on the $2b$ data. The latter is only the Poisson uncertainty on the $2b$ data, in (a), while in (b), it also includes the uncertainty from the bootstrap procedure described in Section 7.

background estimates are produced by applying the CR1-derived weights to three of the SR quadrants, and CR2-derived weights to the one remaining SR quadrant. For example, one alternative background estimate is obtained by applying CR1-derived weights to Q_S , Q_E and Q_W , and CR2-derived weights to Q_N . Each of these four background predictions is symmetrized around the nominal m_{HH} distribution to construct a two-sided uncertainty. Since the m_{HH} distribution differs across the four SR quadrants, substituting the CR2-based prediction for the CR1-based prediction in each of the four SR quadrants separately and utilizing a four-component uncertainty gives the fit model greater flexibility to describe these m_{HH} variations with finer granularity. In the ggF signal region, these uncertainties are taken to be uncorrelated across the datasets from the three different years. In both the ggF and VBF signal regions, the uncertainty is treated as correlated across the analysis categories.

An additional closure uncertainty is estimated by applying the full background modeling procedure to the $3b1f$ sample instead of the $4b$ sample. The predicted $3b1f$ m_{HH} distribution in the various analysis categories is then compared with the observed $3b1f$ data in the SR. For the VBF signal region, no statistically significant difference between the prediction and observation is found, and hence no additional uncertainty is applied. For the ggF signal region, an additional uncertainty is evaluated in each category from the observed differences between the predicted and observed $3b1f$ m_{HH} distributions. For m_{HH} bins in which the predicted and observed values differ by less than 1σ , where σ is obtained from all other background modeling uncertainties combined, no additional uncertainty is applied. For m_{HH} bins where the predicted and observed values differ by more than 1σ , the amount beyond 1σ is averaged with the corresponding amounts in the two adjacent bins, to limit the impact of statistical fluctuations, and is symmetrized around the nominal prediction to construct a two-sided uncertainty. This nonclosure uncertainty has a much smaller impact on the analysis sensitivity than the other sources of background modeling uncertainty.

Several detector modeling uncertainties are evaluated and included. These affect only the signal description, as the background is estimated entirely from data. Uncertainties in the jet energy scale and resolution,

Table 5: A summary of all the data samples used in the analysis. For each control sample, the variations from the nominal analysis are noted explicitly.

Data Sample	Definition	Usage
Signal Region (SR)	Events with $X_{HH} < 1.6$	Defines signal region in the $m_{H1}-m_{H2}$ plane
Control Region (CR)	Events with $X_{HH} > 1.6$ and $R_{CR} < 45$ GeV	Defines control region in the $m_{H1}-m_{H2}$ plane for background estimation (ggF and VBF)
Shifted validation regions	Shift the center of the SR in the $m_{H1}-m_{H2}$ plane to avoid overlap with the nominal SR	Background estimation validation (ggF only)
$4b$	Events with at least 4 b -tagged central jets	Final analysis sample (ggF and VBF)
$2b$	Events with exactly 2 b -tagged central jets plus at least two additional untagged central jets	Background estimation (ggF and VBF)
$3b1f$	Events with exactly 3 b -tagged central jets plus at least one central jet failing a looser b -tagging requirement	Background estimation validation (ggF and VBF), additional background modeling uncertainty (ggF only)
Reverse $ \Delta\eta_{HH} $	$2b$ and $4b$ events with $ \Delta\eta_{HH} > 1.5$	Background estimation validation (ggF only)

as well as the JVT, are treated according to the prescription in Refs. [80, 81]. Additional uncertainties arising from the correction of the simulated pileup distribution are treated according to the prescription in Ref. [95]. Uncertainties in the b -tagging efficiency are treated according to the prescription in Ref. [96]. Uncertainties in the trigger efficiencies are evaluated from measurements of per-jet online efficiencies for both jet reconstruction and b -tagging, which are used to compute event-level uncertainties. These are then applied to the simulated events as overall weight variations. The uncertainty in the integrated luminosity used in this analysis is in the range 2.0%–2.4% for the three years of data taking and 1.7% for the entire dataset [97], obtained using the LUCID-2 detector for the primary luminosity measurements [98].

Several sources of theoretical uncertainty affecting the signal models are considered as described below. Uncertainties due to modeling of the parton shower and underlying event are evaluated by comparing results between two generators for these parts of the calculation: the nominal PYTHIA 8 and the alternative HERWIG 7. This is found to have an effect of roughly 10% on the ggF and VBF signal acceptances, and a negligible impact on the shape of the m_{HH} distributions. The parton showering uncertainty is derived within each analysis SR category; the uncertainty is observed to reach approximately 40% for a given

production mode in some categories in which the acceptance is small for that mode. Uncertainties in the matrix element calculation are evaluated by raising and lowering the factorization and renormalization scales used in the generator by a factor of two, both independently and simultaneously. This results in an effect of typically 2% for both ggF and VBF, with a maximum effect of about 6% in certain analysis categories. PDF uncertainties are evaluated using the PDF4LHC_NLO_MC set [54] by calculating the signal acceptance for each replica and taking the standard deviation. The magnitude of this uncertainty is typically found to be less than 1% in both the ggF and VBF signal acceptances, with a maximum magnitude of approximately 2%. Theoretical uncertainties in the $H \rightarrow b\bar{b}$ branching ratio [14] are included, amounting to an approximately 3.5% overall uncertainty in the signal normalization. The dependence of the branching ratio uncertainty on κ_λ is neglected. Theoretical uncertainties in the ggF and VBF HH cross-sections arising from uncertainties in the PDF and α_s , as well as the choice of renormalization scheme and the scale of the top quark’s mass, are taken from Refs. [11, 14, 99]. The cross-section uncertainties are included in the derivation of the upper limits on the ggF, VBF, and combined HH signal strengths, as well as the likelihood-based constraints on the values of the κ_λ and κ_{2V} modifiers, as presented in Section 8.

An additional signal modeling systematic uncertainty is evaluated for the SMEFT and HEFT measurements. The m_{HH} spectra of reweighted SMEFT/HEFT signal samples are compared against explicitly generated samples for a select number of coefficient variations. A two-component normalization uncertainty is derived by taking the average of the relative deviations across the m_{HH} bins in the ranges of $280 < m_{HH} < 936$ GeV and $m_{HH} > 936$ GeV. The use of separate components in the low- and high- m_{HH} regions prevents the level of agreement in the more populated low- m_{HH} region from overconstraining the uncertainty in the more sparsely populated high- m_{HH} region.

8 Results

The analysis results are obtained using a maximum-likelihood fit performed in bins of reconstructed m_{HH} . For the ggF signal region, the fit is performed simultaneously across the different data-taking years (2016, 2017, and 2018), while for the VBF signal region, the fit is performed inclusively on the data from all years.

The likelihood function used to construct the test statistic has a standard form, consisting of a product of Poisson distributions for the yields in each bin and constraint functions for nuisance parameters describing systematic uncertainties. For uncertainties due to the limited sample size in data or simulation, the constraint is a Poisson distribution. For all other systematic uncertainties, the constraint is a Gaussian distribution. Where systematic uncertainties are deemed to be uncorrelated, independent nuisance parameters are introduced. Uncertainties in the luminosity and signal modeling are treated as fully correlated between the analysis categories and, for ggF, the data-taking years. Each component of the quadrant-derived uncertainty covering the kinematic differences between the SR and CR1 regions is correlated across the data-taking years for the ggF region. The components are correlated across analysis categories within the ggF and VBF signal regions, but not between the ggF and VBF signal regions. All other uncertainties in the background model are treated as uncorrelated across the different categories and data-taking years. The statistical model is implemented using RooFit [100].

The hypothesis of the presence of a signal is tested using the profile likelihood ratio [101]. The signal strength of the combined ggF and VBF signal process, $\mu_{\text{ggF+VBF}} (= \sigma_{\text{ggF+VBF}} / \sigma_{\text{ggF+VBF}}^{\text{SM}})$, is chosen as the parameter of interest (POI) and is a free parameter in the fit. The relative contributions of the ggF and VBF

signals to the total signal model are fixed to their predicted values. The profile likelihood ratio takes the following form:

$$-2\Delta \ln \lambda(\mu) = -2 \ln \left(\frac{L(\mu, \hat{\theta})}{L(\hat{\mu}, \hat{\theta})} \right),$$

where μ is the POI and θ represents the nuisance parameters. The numerator represents the conditional maximum-likelihood fit, in which the nuisance parameters are set to their profiled values $\hat{\theta}$ for which the likelihood is maximized for a fixed value of μ . The denominator represents the unconditional likelihood fit, where both μ and θ are set to the values which jointly maximize the likelihood, $\hat{\mu}$ and $\hat{\theta}$, respectively.

The observed distributions in m_{HH} , as well as the predicted background and example signal shapes, are presented in Figure 7 for each of the six ggF categories (with all data-taking years combined, for presentation purposes). The distributions of the expected background are obtained using the best-fit values of the nuisance parameters in the fit to the data with the background-only hypothesis. The corresponding m_{HH} distributions in the two VBF categories are shown in Figure 8. The signal shape for $\kappa_{2V} = 0$ in Figure 8(a) clearly shows the impact of the divergences in Figures 2(b) and 2(c) not canceling out as discussed in Section 1. While the deviations from the SM studied in this analysis are below the level that violates unitarity, this behavior makes the VBF topology in this analysis particularly sensitive to κ_{2V} . The observed number of data events, predicted number of background events, and expected number of signal events for the SM ggF and VBF signals are summarized for each of the analysis categories in Table 6.

Table 6: The yields in each analysis category of the data, expected background, and expected SM ggF and VBF signals. The expected background yields are obtained using a fit to the data with the background-only hypothesis; the quoted uncertainties are the sum in quadrature of all the per-bin systematic uncertainties. The expected signal yields are obtained from simulation.

Category	Data	Expected Background	ggF Signal SM	VBF Signal SM
ggF signal region				
$ \Delta\eta_{HH} < 0.5, X_{HH} < 0.95$	1940	1935 ± 25	7.0	0.038
$ \Delta\eta_{HH} < 0.5, X_{HH} > 0.95$	3602	3618 ± 37	6.5	0.036
$0.5 < \Delta\eta_{HH} < 1.0, X_{HH} < 0.95$	1924	1874 ± 21	5.1	0.037
$0.5 < \Delta\eta_{HH} < 1.0, X_{HH} > 0.95$	3540	3492 ± 35	4.7	0.040
$ \Delta\eta_{HH} > 1.0, X_{HH} < 0.95$	1880	1739 ± 22	2.9	0.043
$ \Delta\eta_{HH} > 1.0, X_{HH} > 0.95$	3285	3212 ± 37	2.8	0.041
VBF signal region				
$ \Delta\eta_{HH} < 1.5$	116	125.3 ± 4.4	0.37	0.090
$ \Delta\eta_{HH} > 1.5$	241	230.6 ± 5.3	0.06	0.21

An upper limit on the combined ggF and VBF HH signal strength $\mu_{\text{ggF+VBF}}$ is computed using the asymptotic formula [101] and based on the CL_s method [102]. The observed (expected) 95% CL upper limit on $\mu_{\text{ggF+VBF}}$ is found to be 5.4 (8.1). The expected upper limits are obtained using a background-only hypothesis, excluding a HH signal. The upper limit on the combined $\mu_{\text{ggF+VBF}}$, as well as upper limits on the individual μ_{ggF} ($= \sigma_{\text{ggF}}/\sigma_{\text{ggF}}^{\text{SM}}$) and μ_{VBF} ($= \sigma_{\text{VBF}}/\sigma_{\text{VBF}}^{\text{SM}}$), are summarized in Table 7. For the individual μ_{ggF} and μ_{VBF} limits, the results are derived by treating the other production mode (VBF when placing limits on μ_{ggF} , and vice-versa) as a background process, with its normalization only loosely constrained in the fit. Compared to the previous ATLAS measurement of ggF HH production in the $b\bar{b}b\bar{b}$ decay

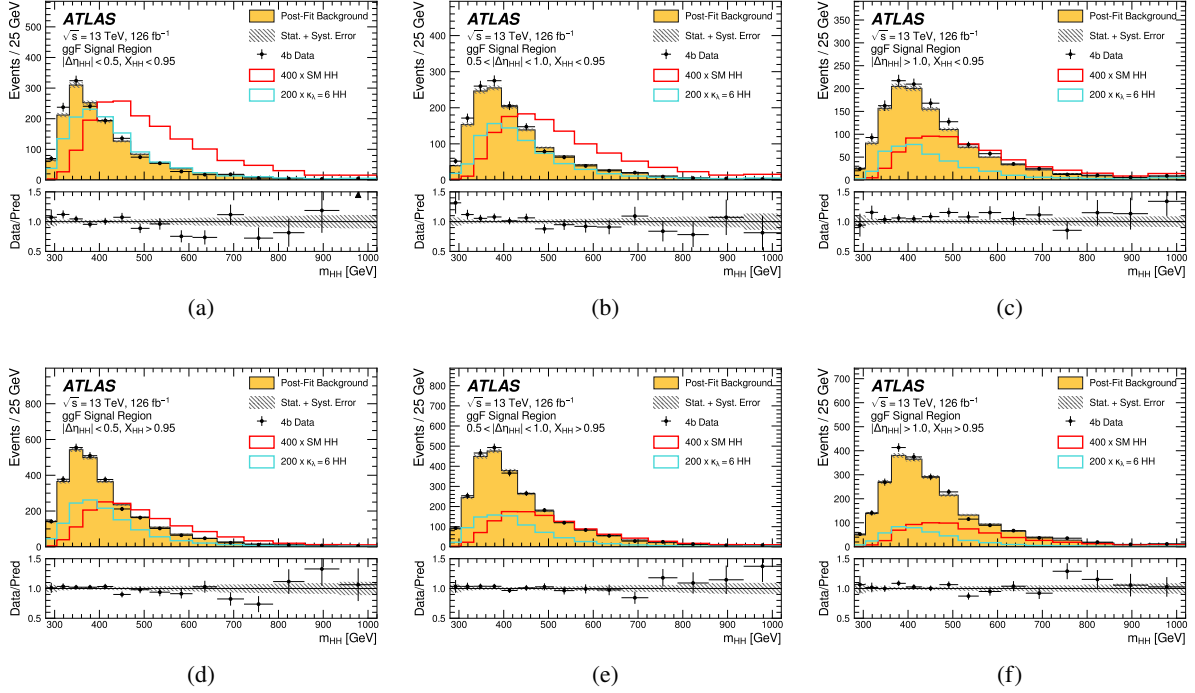


Figure 7: Distributions of the reconstructed m_{HH} in data (shown by the black points) and the estimated background (shown by the yellow histograms), in each of the six $|\Delta\eta_{HH}|, X_{HH}$ categories in the ggF signal region: (a) $|\Delta\eta_{HH}| < 0.5, X_{HH} < 0.95$; (b) $0.5 < |\Delta\eta_{HH}| < 1.0, X_{HH} < 0.95$; (c) $|\Delta\eta_{HH}| > 1.0, X_{HH} < 0.95$; (d) $|\Delta\eta_{HH}| < 0.5, X_{HH} > 0.95$; (e) $0.5 < |\Delta\eta_{HH}| < 1.0, X_{HH} > 0.95$; and (f) $|\Delta\eta_{HH}| > 1.0, X_{HH} > 0.95$. The contributions from the different data-taking years are combined in each category for presentation purposes. The hatching shows the total uncertainty of the background estimate. The distribution of the expected background is obtained using the best-fit values of the nuisance parameters in the fit to the data with the background-only hypothesis. Distributions of the SM and $\kappa_\lambda = 6$ signal models are overlaid, scaled so as to be visible on the plot, and the scaling for each signal model is the same across the six categories. The lower panels show the ratio of the observed data yield to the predicted background in each bin. Events in the underflow and overflow bins are counted in the yields of the initial and final bins respectively.

channel (using 27 fb^{-1} of early Run 2 data) [26], the upper limit on the ggF cross-section is over 50% lower, with approximately 20% of this improvement arising from advances in analysis techniques and object reconstruction. Similarly, compared to the previous ATLAS measurement of VBF HH production in the $b\bar{b}b\bar{b}$ decay channel, which used 126 fb^{-1} of data collected between 2016 and 2018 [27], the upper limit on the VBF HH cross-section is over 75% lower, with this improvement arising entirely from advances in analysis technique and object reconstruction.

The total uncertainty in the upper limit of the cross-section is dominated by the uncertainty sources related to the background modeling procedure and theoretical predictions. With only the statistical uncertainties of the reweighted $2b$ data, observed $4b$ data, and simulated signal samples included in the fit, the expected upper limit on $\mu_{\text{ggF+VBF}}$ is found to be 6.0 times the SM prediction. Including the uncertainty sources resulting from the background estimation (the bootstrap uncertainty, the uncertainty from the kinematic differences between the SR and CR1, and, in the ggF signal region, the $3b1f$ nonclosure uncertainty), the expected upper limit on $\mu_{\text{ggF+VBF}}$ is relaxed to 7.1 times the SM prediction. The further reduction of sensitivity to the value of 8.1, as quoted in Table 7, is driven primarily by the uncertainties arising from theoretical predictions. The relative impact of the various sources of systematic uncertainty on the

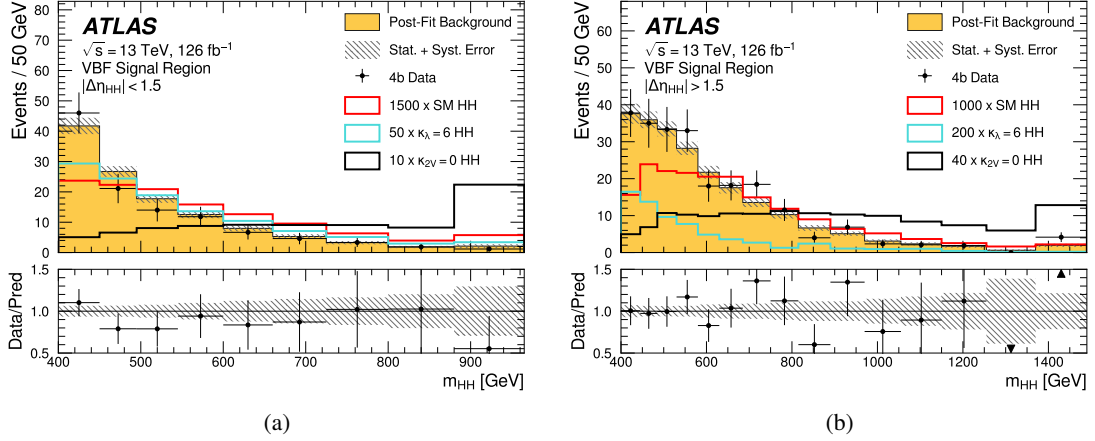


Figure 8: Distributions of the reconstructed m_{HH} in data (shown by the black points), the estimated background (shown by the yellow histograms), in each of the two $|\Delta\eta_{HH}|$ categories in the VBF signal region: (a) $|\Delta\eta_{HH}| < 1.5$ and (b) $|\Delta\eta_{HH}| > 1.5$. The hatching shows the total uncertainty of the background estimate. The distribution of the expected background is obtained using the best-fit values of the nuisance parameters in the fit to the data with the background-only hypothesis. Distributions for three choices of couplings are shown: the SM, $\kappa_\lambda = 6$, and $\kappa_{2V} = 0$ (with all other couplings set to their SM values in the last two models), scaled so as to be visible on the plot. The lower panels show the ratio of the observed data yield to the predicted background in each bin. Events in the overflow bins are counted in the yields of the final bins.

Table 7: The observed and expected upper limits on the SM ggF HH production cross-section σ_{ggF} , SM VBF HH production cross-section σ_{VBF} , and combined SM ggF and VBF HH production cross-section $\sigma_{\text{ggF+VBF}}$ at the 95% CL, expressed as multiples of the corresponding SM cross-sections. The expected values are shown with corresponding one- and two-standard-deviation error bounds, and they are obtained using a background-only fit to the data. When extracting the limits on $\sigma_{\text{ggF+VBF}}$, the relative contributions of ggF and VBF production to the total cross-section are fixed to the SM prediction.

	Observed Limit	-2σ	-1σ	Expected Limit	$+1\sigma$	$+2\sigma$
μ_{ggF}	5.5	4.4	5.9	8.2	12.4	19.6
μ_{VBF}	130	70	100	130	190	280
$\mu_{\text{ggF+VBF}}$	5.4	4.3	5.8	8.1	12.2	19.1

expected upper limit on $\mu_{\text{ggF+VBF}}$ is summarized in Table 8.

Constraints are placed on the κ_λ and κ_{2V} modifiers using two different interpretations, the first named the “95% CL” method and the second named the “profile likelihood ratio” method. The former uses the signal strength μ as the POI, while the latter uses the vector of coupling modifiers $\kappa = (\kappa_\lambda, \kappa_{2V})$. The 95% CL method allows for interpretation as a traditional search for an arbitrarily normalized set of signals with different shapes against an estimated background, while the profile likelihood ratio method allows for interpretation as to whether the data are compatible with the specific cross-section and shape predictions of the κ framework. The 95% CL results presented here offer a consistent comparison with previous ATLAS HH measurements. The constraints obtained from the two interpretations are not expected to be identical, as the two strategies employ slightly different physical assumptions. In the profile likelihood

Table 8: Breakdown of the dominant systematic uncertainties. The impact of the uncertainties on the expected upper limit on $\mu_{\text{ggF+VBF}}$ when re-evaluating the profile likelihood ratio after fixing the nuisance parameter(s) in question to its (their) best-fit value(s), while all remaining nuisance parameters remain free to float. The impact is shown in %. Only (groups of) systematic uncertainties that have an impact of at least 1% are shown. The impact of each experimental source of systematic uncertainty described in the text, as well as of all of them together, is less than 1%.

Source of Uncertainty	$\Delta\mu/\mu$
Theory uncertainties	
Theory uncertainty in signal cross-section	-9.0%
All other theory uncertainties	-1.4%
Background modeling uncertainties	
Bootstrap uncertainty	-7.1%
CR to SR extrapolation uncertainty	-7.5%
3b1f nonclosure uncertainty	-2.0%

ratio interpretation, the signal strength is fixed to the prediction obtained for a specific coupling modifier configuration, while for the 95% CL interpretation, the signal strength is allowed to float. The profile likelihood ratio method utilizes a hypothesis consisting of the predicted background plus the SM HH signal, while the 95% CL results utilize a hypothesis containing only the predicted background and no HH signal. Given the relatively small size of the SM HH signal compared to the predicted background, the use of different hypotheses is not expected to have a significant effect. Additionally, 2σ -level constraints are quoted from the profile likelihood ratio interpretation, as opposed to 95% CL constraints.

The 95% CL constraints on κ_λ and κ_{2V} are obtained by determining the 95% CL upper limits on the cross-section as a function of these coupling modifiers, $\mu_{\text{ggF+VBF}}(\kappa_\lambda, \kappa_{2V})$. Values of the coupling modifiers ($\kappa_\lambda, \kappa_{2V}$) are excluded if the predicted cross-section of the signal model obtained with that configuration is excluded at the 95% CL. The $H \rightarrow b\bar{b}$ branching ratio is fixed to the SM prediction in the likelihood fit and any dependence on κ_λ is ignored. Upper limits on the HH signal strength as a function of κ_λ and κ_{2V} are shown in Figure 9, and the exclusion boundaries are summarized in Table 9. With the values of the other modifiers (κ_V and either κ_{2V} or κ_λ , respectively) fixed to their SM value of 1, values of κ_λ beyond $[-3.9, 11.1]$ and values of κ_{2V} beyond $[-0.03, 2.11]$ are excluded.

Table 9: The observed and expected constraints on the κ_λ and κ_{2V} coupling modifiers at 95% CL. For each modifier, the constraints were extracted with all other modifiers fixed to the SM prediction.

Parameter	Expected Constraint		Observed Constraint	
	Lower	Upper	Lower	Upper
κ_λ	-4.6	10.8	-3.9	11.1
κ_{2V}	-0.05	2.12	-0.03	2.11

Figure 10 shows the 95% CL exclusion limits in the two-dimensional plane of the κ_λ - κ_{2V} modifier space.

The alternative coupling modifier constraints are obtained using the profile likelihood ratio interpretation, with the coupling modifiers $\boldsymbol{\kappa} = (\kappa_\lambda, \kappa_{2V})$ as the POIs, rather than the signal strength μ :

$$-2\Delta \ln L(\boldsymbol{\kappa}) = -2 \ln \left(\frac{L(\boldsymbol{\kappa}, \hat{\boldsymbol{\theta}})}{L(\hat{\boldsymbol{\kappa}}, \hat{\boldsymbol{\theta}})} \right).$$

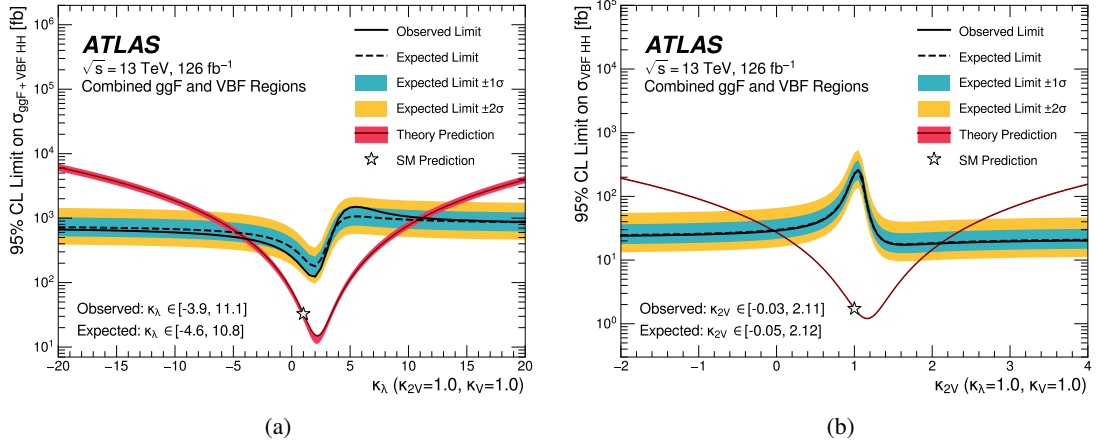


Figure 9: The observed 95% CL exclusion limits as a function of (a) κ_λ (obtained using the signal strength $\mu_{\text{ggF+VBF}}$ as the POI) and (b) κ_{2V} (obtained using the signal strength μ_{VBF} as the POI) from the combined ggF and VBF signal regions, as shown by the solid black line. In each case, the value of the other modifier is fixed to 1. The blue and yellow bands show respectively the 1σ and 2σ bands around the expected exclusion limits, which are shown by the dashed black line. The expected exclusion limits are obtained using a fit to the data with the background-only hypothesis. The dark red line shows in (a) the predicted combined ggF and VBF HH cross-section as a function of κ_λ and in (b) the predicted VBF HH cross-section as a function of κ_{2V} . The dark pink bands surrounding the predicted cross-section lines indicate the theoretical uncertainty of the cross-section, as taken from Ref. [99]. The band in (b) is smaller than the width of the plotted line.

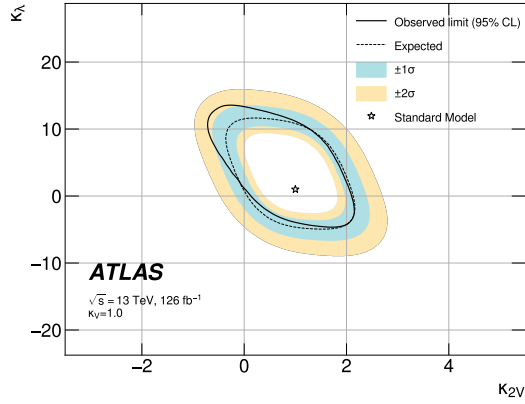


Figure 10: The observed 95% CL exclusion limit obtained using the signal strength $\mu_{\text{ggF+VBF}}$ as the POI in the two-dimensional κ_λ vs. κ_{2V} space, obtained from the combined ggF and VBF signal model, as shown by the solid black line. The blue and yellow bands show respectively the 1σ and 2σ bands around the expected exclusion limits, which are shown by the dashed black line. The star denotes the SM prediction ($\kappa_\lambda = \kappa_{2V} = 1$).

A scan of the profile likelihood ratio is performed as a function of the coupling modifiers at discrete points to produce the curves shown in Figure 11. The best-fit value of κ_λ is found to be 6.2 from the profile likelihood scan. The observed pull of the best-fit κ_λ value away from the SM value is due to a slight excess in the observed data in the ggF signal region, specifically in the low- m_{HH} range. The particular signal model in which κ_λ is close to 6 is favored due to a balance between two competing effects: the m_{HH} spectrum becomes softer as κ_λ increases away from the SM, but the cross-section also grows beyond the

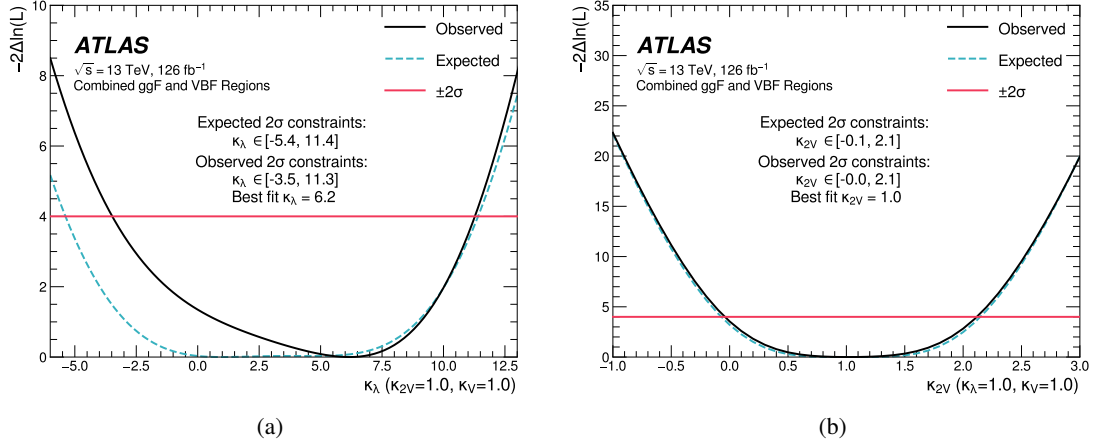


Figure 11: The observed profile likelihood ratio scans for the (a) κ_λ and (b) κ_{2V} coupling modifiers, shown by the solid black line, using the coupling modifiers κ as the POIs. In each case, the value of the other parameter is fixed to 1. The dashed blue line shows the expected profile likelihood ratio, as obtained using a fit to the data with the background-only hypothesis. The pink line indicates the 2σ exclusion boundary.

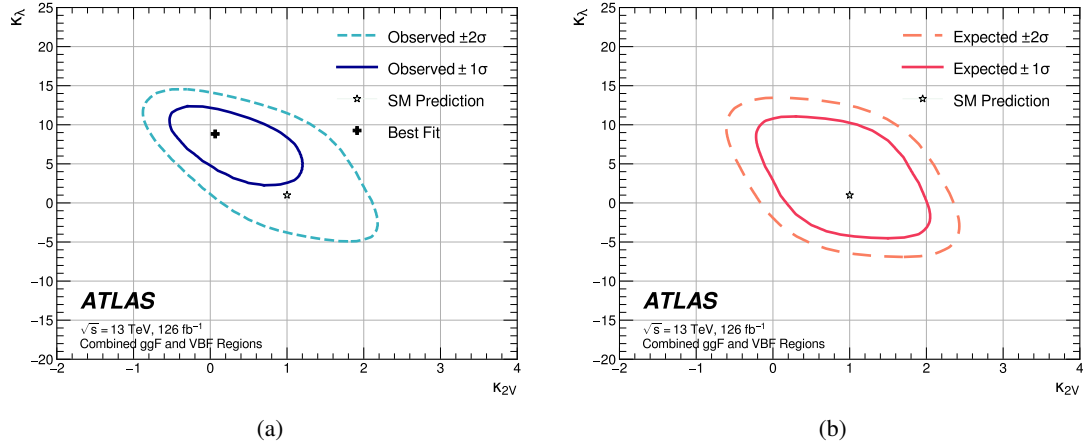


Figure 12: (a) The observed profile likelihood ratio exclusion limits for the two-dimensional κ_λ vs. κ_{2V} modifier space, shown by the solid dark purple line at the 1σ level and the dashed turquoise line at the 2σ level. The black cross denotes the best-fit values of $(\kappa_\lambda, \kappa_{2V})$. The expected exclusion limits are presented in (b), where the solid pink line denotes the 1σ -level exclusion and the dashed orange line denotes the 2σ -level exclusion. For both the expected and observed limit plots, the black star indicates the SM prediction ($\kappa_\lambda = \kappa_{2V} = 1$).

magnitude of the excess as κ_λ increases much further. This slight excess also results in the deviation of the observed limits in Figure 11 from the expected limits by about 1σ . No such excess is observed in the VBF signal region, and the best-fit value of κ_{2V} from the likelihood scan is found to be 1.0. With the values of the other modifiers (κ_V and either κ_{2V} or κ_λ , respectively) fixed to their SM value of 1, the observed (expected) 2σ allowed range for κ_λ is found to be $[-3.5, 11.3]$ ($[-5.4, 11.4]$) and the corresponding range for κ_{2V} is $[-0.0, 2.1]$ ($[-0.1, 2.1]$).

The exclusion constraints obtained using the profile likelihood ratio method are also presented in the

two-dimensional κ_λ - κ_{2V} coupling modifier space, similarly to the 95% CL constraints described above. The excluded regions are presented in Figure 12. With both modifiers able to float in the two-dimensional fit that combines both the ggF and VBF signal regions, the fit converges to κ_λ and κ_{2V} values slightly different from the ones where the minimum is found in the fits with a single parameter free.

In addition to constraints on the ggF and VBF HH cross-sections and the κ_λ and κ_{2V} coupling modifiers, constraints for relevant coefficients can be derived from the ggF selection of the analysis in the SMEFT and HEFT frameworks, as outlined in Section 1. The VBF HH process was ignored for both the SMEFT and HEFT results; including the VBF HH process as a background was found to have a negligible effect on the extracted parameter limits. The slight dependence of the $H \rightarrow b\bar{b}$ branching fraction on the SMEFT and HEFT coefficients is also ignored, as the impact on the analysis sensitivity is small. Constraints on the SMEFT coefficients are extracted by considering the 95% CL exclusion of the cross-section as a function of SMEFT parameter, as was done for the κ_λ and κ_{2V} constraints discussed previously. The extracted constraints on individual parameters in the scenario where the other parameters are fixed to 0 are summarized in Table 10. Limits approaching or exceeding $\pm 4\pi$ should be interpreted with caution because of the potential impact from effects such as missing higher-order model contributions. The exclusion limits are also presented in two-dimensional SMEFT coefficient subspaces. The exclusion limits for each coefficient versus the c_H coefficient (with the remaining three coefficients fixed to 0) are shown in Figure 13. The upper limits on the HEFT ggF HH production cross-section in the seven benchmark models are presented in Figure 14. The spread of sensitivity between the seven benchmark models reflects the different signal kinematics and, hence, shapes of the signal m_{HH} distributions. The different variation between observed and expected limits is linked to the slight excess observed in the low m_{HH} region, as discussed earlier. The red crosses in Figure 14 indicate the predicted HH cross-sections from the respective benchmark models. As can be seen, BM3, BM5 and BM7 are observed to be excluded with more than 95% confidence. Constraints are placed on the values of c_{ggHH} and $c_{t\bar{t}HH}$, with all other HEFT coefficients fixed to SM values. The observed (expected) constraints on c_{ggHH} are found to be $[-0.36, 0.78]$ ($[-0.42, 0.75]$), while the observed (expected) constraints on $c_{t\bar{t}HH}$ are found to be $[-0.55, 0.51]$ ($[-0.46, 0.40]$).

Table 10: The extracted upper and lower limits on the SMEFT parameters to which the analysis is sensitive. For each parameter, the constraints are provided assuming the other parameters are fixed to 0. The VBF HH process is ignored for this result.

Parameter	Expected Constraint		Observed Constraint	
	Lower	Upper	Lower	Upper
c_H	-20	11	-22	11
c_{HG}	-0.056	0.049	-0.067	0.060
$c_{H\Box}$	-9.3	13.9	-8.9	14.5
c_{tH}	-10.0	6.4	-10.7	6.2
c_{tG}	-0.97	0.94	-1.12	1.15

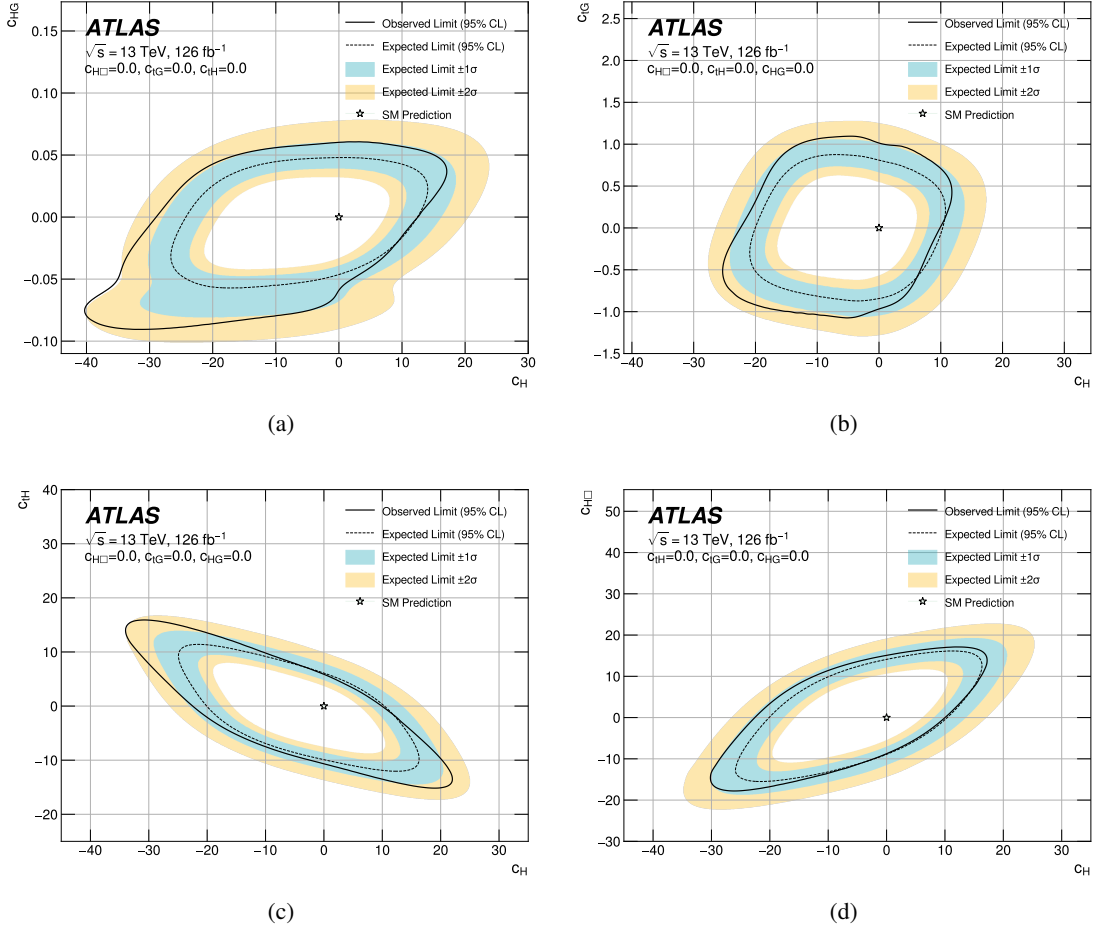


Figure 13: The observed 95% CL exclusion limits on the SMEFT coefficients in the two-dimensional spaces (a) c_{HG} vs. c_H , (b) c_{IG} vs. c_H , (c) c_{IH} vs. c_H , and (d) c_{HD} vs. c_H , shown by the solid black lines. The dashed black line indicates the expected 95% CL exclusion limits. The shaded blue band indicates the $\pm 1\sigma$ uncertainty of the exclusion limits, while the yellow band indicates the $\pm 2\sigma$ uncertainty. The values of the other three coefficients for each plot are fixed to 0. The VBF HH process is ignored for this result.

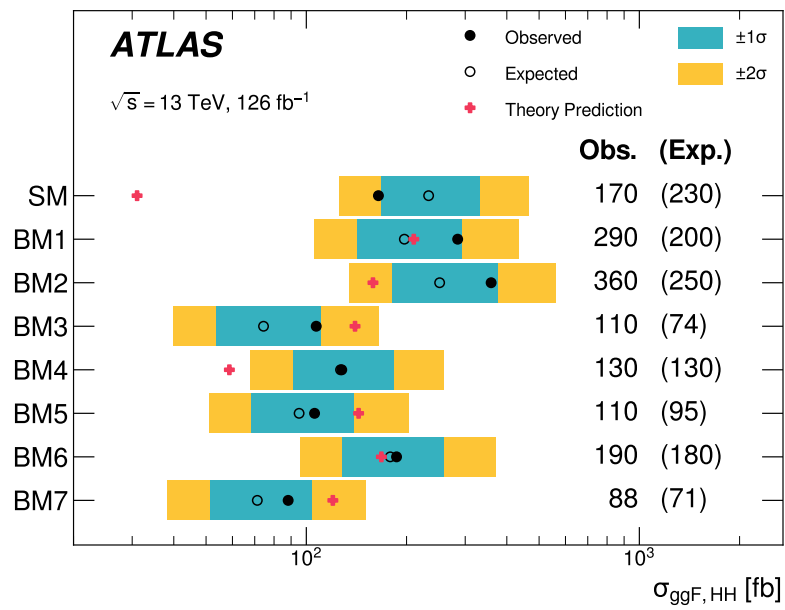


Figure 14: The observed 95% CL exclusion limits on the ggF HH production cross-section in the SM and each of the seven HEFT benchmark models, given by the solid black points. The blue and yellow bands show respectively the 1σ and 2σ bands around the expected upper limits, which are shown by the open circles. The predicted ggF HH production cross-section from each benchmark is indicated by a pink cross. The VBF HH process is ignored for this result.

9 Conclusion

A search for nonresonant pair production of Higgs bosons in the $b\bar{b}b\bar{b}$ final state was carried out, with dedicated analyses for the ggF and VBF production modes, using 126 fb^{-1} of $\sqrt{s} = 13 \text{ TeV}$ pp collision data collected by the ATLAS detector at the LHC. The sensitivity of the analyses is improved relative to previous iterations by using more sophisticated background modeling techniques, event categorization and improved jet reconstruction and flavor identification algorithms, in addition to the increased integrated luminosity of the analyzed data.

No evidence of signal is found and the observed (expected) upper limit on the cross-section for nonresonant Higgs boson pair production is determined to be 5.4 (8.1) times the Standard Model predicted cross-section at 95% confidence level. Constraints are placed upon modifiers to the HHH and $HHVV$ couplings. The observed (expected) 2σ constraints on the HHH coupling modifier, κ_λ , are determined to be $[-3.5, 11.3]$ ($[-5.4, 11.4]$), while the corresponding constraints for the $HHVV$ coupling modifier, κ_{2V} , are $[-0.0, 2.1]$ ($[-0.1, 2.1]$). The results are also used to derive constraints on relevant coefficients in the SM effective field theory and the Higgs effective field theory frameworks.

References

- [1] ATLAS Collaboration, *Observation of a new particle in the search for the Standard Model Higgs boson with the ATLAS detector at the LHC*, *Phys. Lett. B* **716** (2012) 1, arXiv: [1207.7214 \[hep-ex\]](#).
- [2] CMS Collaboration, *Observation of a new boson at a mass of 125 GeV with the CMS experiment at the LHC*, *Phys. Lett. B* **716** (2012) 30, arXiv: [1207.7235 \[hep-ex\]](#).
- [3] ATLAS Collaboration, *Observation of $H \rightarrow b\bar{b}$ decays and VH production with the ATLAS detector*, *Phys. Lett. B* **786** (2018) 59, arXiv: [1808.08238 \[hep-ex\]](#).
- [4] CMS Collaboration, *Observation of Higgs Boson Decay to Bottom Quarks*, *Phys. Rev. Lett.* **121** (2018) 121801, arXiv: [1808.08242 \[hep-ex\]](#).
- [5] G. C. Branco et al., *Theory and phenomenology of two-Higgs-doublet models*, *Phys. Rept.* **516** (2012) 1, arXiv: [1106.0034 \[hep-ph\]](#).
- [6] R. Gröber and M. Mühlleitner, *Composite Higgs boson pair production at the LHC*, *JHEP* **06** (2011) 020, arXiv: [1012.1562 \[hep-ph\]](#).
- [7] Z. Chacko, Y. Nomura, M. Papucci, and G. Perez, *Natural little hierarchy from a partially goldstone twin Higgs*, *JHEP* **01** (2006) 126, arXiv: [hep-ph/0510273](#).
- [8] P. Fayet, *Supersymmetry and weak, electromagnetic and strong interactions*, *Phys. Lett. B* **64** (1976) 159.
- [9] P. Fayet, *Spontaneously broken supersymmetric theories of weak, electromagnetic and strong interactions*, *Phys. Lett. B* **69** (1977) 489.

- [10] G. Degrandi et al., *Higgs mass and vacuum stability in the Standard Model at NNLO*, *JHEP* **08** (2012) 098, arXiv: [1205.6497](#).
- [11] M. Grazzini et al., *Higgs boson pair production at NNLO with top quark mass effects*, *JHEP* **05** (2018) 059, arXiv: [1803.02463](#) [[hep-ph](#)].
- [12] F. A. Dreyer and A. Karlberg, *Vector-boson fusion Higgs pair production at N^3LO* , *Phys. Rev. D* **98** (2018) 114016, arXiv: [1811.07906](#) [[hep-ph](#)].
- [13] F. Bishara, R. Contino, and J. Rojo, *Higgs pair production in vector-boson fusion at the LHC and beyond*, *Eur. Phys. J. C* **77** (2017) 481, arXiv: [1611.03860](#) [[hep-ph](#)].
- [14] D. de Florian et al., *Handbook of LHC Higgs Cross Sections: 4. Deciphering the Nature of the Higgs Sector*, (2016), arXiv: [1610.07922](#) [[hep-ph](#)].
- [15] A. Djouadi, J. Kalinowski, and M. Spira, *HDECAY: A program for Higgs boson decays in the Standard Model and its supersymmetric extension*, *Comput. Phys. Commun.* **108** (1998) 56, arXiv: [hep-ph/9704448](#).
- [16] W. Buchmuller and D. Wyler, *Effective lagrangian analysis of new interactions and flavour conservation*, *Nucl. Phys. B* **268** (1986) 621.
- [17] C. N. Leung, S. T. Love, and S. Rao, *Low-energy manifestations of a new interactions scale: Operator analysis*, *Z. Phys. C* **31** (1986) 433.
- [18] I. Brivio and M. Trott, *The standard model as an effective field theory*, *Phys. Rept.* **793** (2019) 1, arXiv: [1706.08945](#) [[hep-ph](#)].
- [19] R. Alonso, M. Gavela, L. Merlo, S. Rigolin, and J. Yepes, *The effective chiral lagrangian for a light dynamical "Higgs particle"*, *Phys. Lett. B* **722** (2012) 330, arXiv: [1212.3305](#) [[hep-ph](#)].
- [20] G. Buchalla, O. Catà, and C. Krause, *Complete electroweak chiral Lagrangian with a light Higgs at NLO*, *Nucl. Phys. B* **880** (2014) 552, arXiv: [1307.5017](#) [[hep-ph](#)], Erratum: *Nucl. Phys. B* **913** (2016) 475.
- [21] B. Grzadkowski, M. Iskrzynski, M. Misiak, and J. Rosiek, *Dimension-six terms in the Standard Model Lagrangian*, *JHEP* **10** (2010) 085, arXiv: [1008.4884](#) [[hep-ph](#)].
- [22] ATLAS Collaboration, *Combined effective field theory interpretation of Higgs boson and weak boson production and decay with ATLAS data and electroweak precision observables*, ATL-PHYS-PUB-2022-037, 2022, URL: <https://cds.cern.ch/record/2816369>.
- [23] G. Buchalla, O. Catà, and C. Krause, *On the power counting in effective field theories*, *Phys. Lett. B* **731** (2014) 80, arXiv: [1312.5624](#) [[hep-ph](#)].
- [24] M. Capozzi and G. Heinrich, *Exploring anomalous couplings in Higgs boson pair production through shape analysis*, *JHEP* **03** (2020) 091, arXiv: [1908.08923](#) [[hep-ph](#)].
- [25] A. Carvalho et al., *Higgs pair production: choosing benchmarks with cluster analysis*, *JHEP* **04** (2016) 126, arXiv: [1507.02245](#) [[hep-ph](#)].

- [26] ATLAS Collaboration, *Search for pair production of Higgs bosons in the $b\bar{b}b\bar{b}$ final state using proton–proton collisions at $\sqrt{s} = 13$ TeV with the ATLAS detector*, *JHEP* **01** (2019) 030, arXiv: [1804.06174 \[hep-ex\]](#).
- [27] ATLAS Collaboration, *Search for the $HH \rightarrow b\bar{b}b\bar{b}$ process via vector-boson fusion production using proton–proton collisions at $\sqrt{s} = 13$ TeV with the ATLAS detector*, *JHEP* **07** (2020) 108, arXiv: [2001.05178 \[hep-ex\]](#), [Erratum: *JHEP* **01** (2021) 145].
- [28] CMS Collaboration, *Search for Higgs Boson Pair Production in the Four b Quark Final State in Proton-Proton Collisions at $s=13$ TeV*, *Phys. Rev. Lett.* **129** (2022) 081802, arXiv: [2202.09617 \[hep-ex\]](#).
- [29] CMS Collaboration, *Search for nonresonant pair production of highly energetic Higgs bosons decaying to bottom quarks*, (2022), arXiv: [2205.06667 \[hep-ex\]](#).
- [30] ATLAS Collaboration, *Search for resonant and non-resonant Higgs boson pair production in the $b\bar{b}\tau^+\tau^-$ decay channel using 13 TeV pp collision data from the ATLAS detector*, (2022), arXiv: [2209.10910 \[hep-ex\]](#).
- [31] CMS Collaboration, *Search for Higgs boson pair production in events with two bottom quarks and two tau leptons in proton–proton collisions at $\sqrt{s} = 13$ TeV*, *Phys. Lett. B* **778** (2018) 101, arXiv: [1707.02909 \[hep-ex\]](#).
- [32] ATLAS Collaboration, *Search for Higgs boson pair production in the two bottom quarks plus two photons final state in pp collisions at $\sqrt{s} = 13$ TeV with the ATLAS detector*, *Phys. Rev. D* **106** (2021) 052001, arXiv: [2112.11876 \[hep-ex\]](#).
- [33] CMS Collaboration, *Search for nonresonant Higgs boson pair production in final states with two bottom quarks and two photons in proton–proton collisions at $\sqrt{s} = 13$ TeV*, *JHEP* **03** (2021) 257, arXiv: [2011.12373 \[hep-ex\]](#).
- [34] ATLAS Collaboration, *Search for non-resonant Higgs boson pair production in the $b\bar{b}\ell\nu\ell\nu$ final state with the ATLAS detector in pp collisions at $\sqrt{s} = 13$ TeV*, *Phys. Lett. B* **801** (2020) 135145, arXiv: [1908.06765 \[hep-ex\]](#).
- [35] CMS Collaboration, *Search for resonant and nonresonant Higgs boson pair production in the $b\bar{b}\ell\nu\ell\nu$ final state in proton–proton collisions at $\sqrt{s} = 13$ TeV*, *JHEP* **01** (2018) 054, arXiv: [1708.04188 \[hep-ex\]](#).
- [36] ATLAS Collaboration, *Search for Higgs boson pair production in the $b\bar{b}WW^*$ decay mode at $\sqrt{s} = 13$ TeV with the ATLAS detector*, *JHEP* **04** (2019) 092, arXiv: [1811.04671 \[hep-ex\]](#).
- [37] ATLAS Collaboration, *Search for Higgs boson pair production in the $\gamma\gamma WW^*$ channel using pp collision data recorded at $\sqrt{s} = 13$ TeV with the ATLAS detector*, *Eur. Phys. J. C* **78** (2018) 1007, arXiv: [1807.08567 \[hep-ex\]](#).
- [38] ATLAS Collaboration, *Search for Higgs boson pair production in the $WW^{(*)}WW^{(*)}$ decay channel using ATLAS data recorded at $\sqrt{s} = 13$ TeV*, *JHEP* **05** (2019) 124, arXiv: [1811.11028 \[hep-ex\]](#).
- [39] CMS Collaboration, *A portrait of the Higgs boson by the CMS experiment ten years after the discovery*, *Nature* **607** (2022) 60, arXiv: [2207.00043 \[hep-ex\]](#).
- [40] ATLAS Collaboration, *The ATLAS Experiment at the CERN Large Hadron Collider*, *JINST* **3** (2008) S08003.

- [41] ATLAS Collaboration, *ATLAS Insertable B-Layer: Technical Design Report*, ATLAS-TDR-19; CERN-LHCC-2010-013, 2010, URL: <https://cds.cern.ch/record/1291633>, Addendum: ATLAS-TDR-19-ADD-1; CERN-LHCC-2012-009, 2012, URL: <https://cds.cern.ch/record/1451888>.
- [42] B. Abbott et al., *Production and integration of the ATLAS Insertable B-Layer*, *JINST* **13** (2018) T05008, arXiv: [1803.00844](https://arxiv.org/abs/1803.00844) [[physics.ins-det](#)].
- [43] ATLAS Collaboration, *Performance of the ATLAS trigger system in 2015*, *Eur. Phys. J. C* **77** (2017) 317, arXiv: [1611.09661](https://arxiv.org/abs/1611.09661) [[hep-ex](#)].
- [44] ATLAS Collaboration, *The ATLAS Collaboration Software and Firmware*, ATL-SOFT-PUB-2021-001, 2021, URL: <https://cds.cern.ch/record/2767187>.
- [45] ATLAS Collaboration, *ATLAS data quality operations and performance for 2015–2018 data-taking*, *JINST* **15** (2020) P04003, arXiv: [1911.04632](https://arxiv.org/abs/1911.04632) [[physics.ins-det](#)].
- [46] ATLAS Collaboration, *Configuration and performance of the ATLAS b-jet triggers in Run 2*, *Eur. Phys. J. C* **81** (2021) 1087, arXiv: [2106.03584](https://arxiv.org/abs/2106.03584) [[hep-ex](#)].
- [47] M. Cacciari, G. P. Salam, and G. Soyez, *The anti- k_t jet clustering algorithm*, *JHEP* **04** (2008) 063, arXiv: [0802.1189](https://arxiv.org/abs/0802.1189) [[hep-ph](#)].
- [48] M. Cacciari, G. P. Salam, and G. Soyez, *FastJet user manual*, *Eur. Phys. J. C* **72** (2012) 1896, arXiv: [1111.6097](https://arxiv.org/abs/1111.6097) [[hep-ph](#)].
- [49] ATLAS Collaboration, *The ATLAS Simulation Infrastructure*, *Eur. Phys. J. C* **70** (2010) 823, arXiv: [1005.4568](https://arxiv.org/abs/1005.4568) [[physics.ins-det](#)].
- [50] GEANT4 Collaboration, S. Agostinelli, et al., *GEANT4 – a simulation toolkit*, *Nucl. Instrum. Meth. A* **506** (2003) 250.
- [51] P. Nason, *A New method for combining NLO QCD with shower Monte Carlo algorithms*, *JHEP* **11** (2004) 040, arXiv: [hep-ph/0409146](https://arxiv.org/abs/hep-ph/0409146) [[hep-ph](#)].
- [52] S. Frixione, P. Nason and C. Oleari, *Matching NLO QCD computations with parton shower simulations: the POWHEG method*, *JHEP* **11** (2007) 070, arXiv: [0709.2092](https://arxiv.org/abs/0709.2092) [[hep-ph](#)].
- [53] S. Alioli, P. Nason, C. Oleari, and E. Re, *A general framework for implementing NLO calculations in shower Monte Carlo programs: the POWHEG BOX*, *JHEP* **06** (2010) 043, arXiv: [1002.2581](https://arxiv.org/abs/1002.2581) [[hep-ph](#)].
- [54] J. Butterworth et al., *PDF4LHC recommendations for LHC Run II*, *J. Phys. G* **43** (2016) 023001, arXiv: [1510.03865](https://arxiv.org/abs/1510.03865) [[hep-ph](#)].
- [55] T. Sjöstrand et al., *An introduction to PYTHIA 8.2*, *Comput. Phys. Commun.* **191** (2015) 159, arXiv: [1410.3012](https://arxiv.org/abs/1410.3012) [[hep-ph](#)].
- [56] ATLAS Collaboration, *ATLAS Pythia 8 tunes to 7 TeV data*, ATL-PHYS-PUB-2014-021, 2014, URL: <https://cds.cern.ch/record/1966419>.
- [57] R. D. Ball et al., *Parton distributions with LHC data*, *Nucl. Phys. B* **867** (2013) 244, arXiv: [1207.1303](https://arxiv.org/abs/1207.1303) [[hep-ph](#)].
- [58] ATLAS Collaboration, *Validation of signal Monte Carlo event generation in searches for Higgs boson pairs with the ATLAS detector*, ATL-PHYS-PUB-2019-007, 2019, URL: <https://cds.cern.ch/record/2665057>.

- [59] M. Bähr et al., *Herwig++ Physics and Manual*, *Eur. Phys. J. C* **58** (2008) 639, arXiv: [0803.0883 \[hep-ph\]](#).
- [60] S. Gieseke, C. Röhr, and A. Siodmok, *Colour reconnections in Herwig++*, *Eur. Phys. J. C* **72** (2012) 2225, arXiv: [1206.0041 \[hep-ph\]](#).
- [61] L. A. Harland-Lang, A. D. Martin, P. Motylinski, and R. S. Thorne, *Parton distributions in the LHC era: MMHT 2014 PDFs*, *Eur. Phys. J. C* **75** (2015) 204, arXiv: [1412.3989 \[hep-ph\]](#).
- [62] ATLAS Collaboration, *A study of optimal parameter setting for MADGRAPH5_AMC@NLO + PYTHIA 8 matched setup*, ATL-PHYS-PUB-2015-048, 2015, URL: <https://cds.cern.ch/record/2103221>.
- [63] J. Alwall et al., *The automated computation of tree-level and next-to-leading order differential cross sections, and their matching to parton shower simulations*, *JHEP* **07** (2014) 079, arXiv: [1405.0301 \[hep-ph\]](#).
- [64] J. Alwall, M. Herquet, F. Maltoni, O. Mattelaer, and T. Stelzer, *MadGraph 5 : Going Beyond*, *JHEP* **06** (2011) 128, arXiv: [1106.0522 \[hep-ph\]](#).
- [65] C. Degrande et al., *Automated one-loop computations in the standard model effective field theory*, *Phys. Rev. D* **103** (2021) 096024, arXiv: [2008.11743 \[hep-ph\]](#).
- [66] G. Buchalla, M. Capozzi, A. Celis, G. Heinrich, and L. Scyboz, *Higgs boson pair production in non-linear Effective Field Theory with full m_t -dependence at NLO QCD*, *JHEP* **09** (2018) 057, arXiv: [1806.05162 \[hep-ph\]](#).
- [67] ATLAS Collaboration, *HEFT interpretations of Higgs boson pair searches in $b\bar{b}\gamma\gamma$ and $b\bar{b}\tau^+\tau^-$ final states and of their combination in ATLAS*, ATL-PHYS-PUB-2022-019, 2022, URL: <https://cds.cern.ch/record/2806411>.
- [68] R. D. Ball et al., *Parton distributions for the LHC run II*, *JHEP* **04** (2015) 040, arXiv: [1410.8849 \[hep-ph\]](#).
- [69] ATLAS Collaboration, *Combination of searches for Higgs boson pairs in pp collisions at $\sqrt{s} = 13$ TeV with the ATLAS detector*, *Phys. Lett. B* **800** (2020) 135103, arXiv: [1906.02025 \[hep-ex\]](#).
- [70] J. Baglio et al., *The measurement of the Higgs self-coupling at the LHC: theoretical status*, *JHEP* **04** (2013) 151, arXiv: [1212.5581 \[hep-ph\]](#).
- [71] L.-S. Ling et al., *NNLO QCD corrections to Higgs pair production via vector boson fusion at hadron colliders*, *Phys. Rev. D* **89** (2014) 073001, arXiv: [1401.7754 \[hep-ph\]](#).
- [72] F. A. Dreyer and A. Karlberg, *Fully differential Vector-Boson Fusion Higgs Pair Production at Next-to-Next-to-Leading Order*, *Phys. Rev. D* **99** (2019) 074028, arXiv: [1811.07918 \[hep-ph\]](#).
- [73] J. M. Campbell, R. K. Ellis, P. Nason, and E. Re, *Top-pair production and decay at NLO matched with parton showers*, *JHEP* **04** (2015) 114, arXiv: [1412.1828 \[hep-ph\]](#).
- [74] M. Czakon and A. Mitov, *Top++: A program for the calculation of the top-pair cross-section at hadron colliders*, *Comput. Phys. Commun.* **185** (2014) 2930, arXiv: [1112.5675 \[hep-ph\]](#).

- [75] ATLAS Collaboration, *Improvements in $t\bar{t}$ modelling using NLO+PS Monte Carlo generators for Run 2*, ATL-PHYS-PUB-2018-009, 2018, URL: <https://cds.cern.ch/record/2630327>.
- [76] ATLAS Collaboration, *The Pythia 8 A3 tune description of ATLAS minimum bias and inelastic measurements incorporating the Donnachie–Landshoff diffractive model*, ATL-PHYS-PUB-2016-017, 2016, URL: <https://cds.cern.ch/record/2206965>.
- [77] D. J. Lange, *The EvtGen particle decay simulation package*, *Nucl. Instrum. Meth. A* **462** (2001) 152.
- [78] ATLAS Collaboration, *Vertex Reconstruction Performance of the ATLAS Detector at $\sqrt{s} = 13$ TeV*, ATL-PHYS-PUB-2015-026, 2015, URL: <https://cds.cern.ch/record/2037717>.
- [79] ATLAS Collaboration, *Jet reconstruction and performance using particle flow with the ATLAS Detector*, *Eur. Phys. J. C* **77** (2017) 466, arXiv: [1703.10485](https://arxiv.org/abs/1703.10485) [hep-ex].
- [80] ATLAS Collaboration, *Jet energy scale and resolution measured in proton–proton collisions at $\sqrt{s} = 13$ TeV with the ATLAS detector*, *Eur. Phys. J. C* **81** (2020) 689, arXiv: [2007.02645](https://arxiv.org/abs/2007.02645) [hep-ex].
- [81] ATLAS Collaboration, *Performance of pile-up mitigation techniques for jets in pp collisions at $\sqrt{s} = 8$ TeV using the ATLAS detector*, *Eur. Phys. J. C* **76** (2016) 581, arXiv: [1510.03823](https://arxiv.org/abs/1510.03823) [hep-ex].
- [82] ATLAS Collaboration, *Topological cell clustering in the ATLAS calorimeters and its performance in LHC Run 1*, *Eur. Phys. J. C* **77** (2017) 490, arXiv: [1603.02934](https://arxiv.org/abs/1603.02934) [hep-ex].
- [83] ATLAS Collaboration, *Selection of jets produced in 13 TeV proton–proton collisions with the ATLAS detector*, ATL-CONF-2015-029, 2015, URL: <https://cds.cern.ch/record/2037702>.
- [84] ATLAS Collaboration, *ATLAS flavour-tagging algorithms for the LHC Run 2 pp collision dataset*, (2022), arXiv: [2211.16345](https://arxiv.org/abs/2211.16345) [physics.data-an].
- [85] ATLAS Collaboration, *Calibration of light-flavour b -jet mistagging rates using ATLAS proton–proton collision data at $\sqrt{s} = 13$ TeV*, ATL-CONF-2018-006, 2018, URL: <https://cds.cern.ch/record/2314418>.
- [86] ATLAS Collaboration, *Measurement of the c -jet mistagging efficiency in $t\bar{t}$ events using pp collision data at $\sqrt{s} = 13$ TeV collected with the ATLAS detector*, *Eur. Phys. J. C* **82** (2022) 95, arXiv: [2109.10627](https://arxiv.org/abs/2109.10627) [hep-ex].
- [87] ATLAS Collaboration, *Muon reconstruction and identification efficiency in ATLAS using the full Run 2 pp collision data set at $\sqrt{s} = 13$ TeV*, *Eur. Phys. J. C* **81** (2021) 578, arXiv: [2012.00578](https://arxiv.org/abs/2012.00578) [hep-ex].
- [88] ATLAS Collaboration, *Evidence for the $H \rightarrow b\bar{b}$ decay with the ATLAS detector*, *JHEP* **12** (2017) 024, arXiv: [1708.03299](https://arxiv.org/abs/1708.03299) [hep-ex].
- [89] ATLAS Collaboration, *Muon reconstruction performance of the ATLAS detector in proton–proton collision data at $\sqrt{s} = 13$ TeV*, *Eur. Phys. J. C* **76** (2016) 292, arXiv: [1603.05598](https://arxiv.org/abs/1603.05598) [hep-ex].
- [90] G. V. Moustakides and K. Basioti, *Training Neural Networks for Likelihood/Density Ratio Estimation*, 2019, arXiv: [1911.00405](https://arxiv.org/abs/1911.00405) [eess.SP].

- [91] T. Kanamori, S. Hido, and M. Sugiyama, *A Least-squares Approach to Direct Importance Estimation*, *Journal of Machine Learning Research* **10** (2009) 1391, URL: <http://jmlr.org/papers/v10/kanamori09a.html>.
- [92] V. Nair and G. E. Hinton, “Rectified Linear Units Improve Restricted Boltzmann Machines,” *Proceedings of the 27th International Conference on International Conference on Machine Learning*, ICML’10, Haifa, Israel: Omnipress, 2010 807, ISBN: 9781605589077, URL: <https://dl.acm.org/doi/10.5555/3104322.3104425>.
- [93] B. Lakshminarayanan, A. Pritzel, and C. Blundell, *Simple and Scalable Predictive Uncertainty Estimation using Deep Ensembles*, 2017, arXiv: [1612.01474](https://arxiv.org/abs/1612.01474) [stat.ML].
- [94] B. Efron, *Bootstrap Methods: Another Look at the Jackknife*, *Ann. Statist.* **7** (1979) 1.
- [95] ATLAS Collaboration, *Measurement of the Inelastic Proton–Proton Cross Section at $\sqrt{s} = 13$ TeV with the ATLAS Detector at the LHC*, *Phys. Rev. Lett.* **117** (2016) 182002, arXiv: [1606.02625](https://arxiv.org/abs/1606.02625) [hep-ex].
- [96] ATLAS Collaboration, *ATLAS b -jet identification performance and efficiency measurement with $t\bar{t}$ events in pp collisions at $\sqrt{s} = 13$ TeV*, *Eur. Phys. J. C* **79** (2019) 970, arXiv: [1907.05120](https://arxiv.org/abs/1907.05120) [hep-ex].
- [97] ATLAS Collaboration, *Luminosity determination in pp collisions at $\sqrt{s} = 13$ TeV using the ATLAS detector at the LHC*, ATLAS-CONF-2019-021, 2019, URL: <https://cds.cern.ch/record/2677054>.
- [98] G. Avoni et al., *The new LUCID-2 detector for luminosity measurement and monitoring in ATLAS*, *JINST* **13** (2018) P07017.
- [99] J. Baglio et al., *$gg \rightarrow HH$: Combined uncertainties*, *Phys. Rev. D* **103** (2021) 056002, arXiv: [2008.11626](https://arxiv.org/abs/2008.11626) [hep-ph].
- [100] W. Verkerke and D. Kirkby, *The RooFit toolkit for data modeling*, 2003, arXiv: [physics/0306116](https://arxiv.org/abs/physics/0306116) [physics.data-an].
- [101] G. Cowan, K. Cranmer, E. Gross, and O. Vitells, *Asymptotic formulae for likelihood-based tests of new physics*, *Eur. Phys. J. C* **71** (2011) 1554, arXiv: [1007.1727](https://arxiv.org/abs/1007.1727) [physics.data-an], Erratum: *Eur. Phys. J. C* **73** (2013) 2501.
- [102] A. L. Read, *Presentation of search results: the CL_S technique*, *J. Phys. G* **28** (2002) 2693.